MNRAS 000, 1–19 (2023) Preprint 20 November 2023 Compiled using MNRAS LaTeX style file v3.0

Numerical viscosity and resistivity in MHD turbulence simulations

Lakshmi Malvadi Shivakumar,[1,2]★ Christoph Federrath[1,3]†
[1]Research School of Astronomy & Astrophysics, Australian National University, Canberra, ACT 2611, Australia
[2]Indian Institute of Science, Bangalore 560012, India
[3]Australian Research Council Centre of Excellence in All Sky Astrophysics (ASTRO3D), Canberra, ACT 2611, Australia

arXiv:2311.10350v1 [astro-ph.SR] 17 Nov 2023

Accepted XXX. Received YYY; in original form ZZZ

ABSTRACT

To ensure that magnetohydrodynamical (MHD) turbulence simulations accurately reflect the physics, it is critical to understand numerical dissipation. Here we determine the hydrodynamic and magnetic Reynolds number (Re and Rm) as a function of linear grid resolution N, in MHD simulations with purely numerical viscosity and resistivity (implicit large eddy simulations; ILES). We quantify the numerical viscosity in the subsonic and supersonic regime, via simulations with sonic Mach numbers of $\mathcal{M} = 0.1$ and $\mathcal{M} = 10$, respectively. We find $\mathrm{Re} = (N/N_{\mathrm{Re}})^{p_{\mathrm{Re}}}$, with $p_{\mathrm{Re}} \in [1.2, 1.4]$ and $N_{\mathrm{Re}} \in [0.8, 1.7]$ for $\mathcal{M} = 0.1$, and $p_{\mathrm{Re}} \in [1.5, 2.0]$ and $N_{\mathrm{Re}} \in [0.8, 4.4]$ for $\mathcal{M} = 10$, and we find $\mathrm{Rm} = (N/N_{\mathrm{Rm}})^{p_{\mathrm{Rm}}}$, with $p_{\mathrm{Rm}} \in [1.3, 1.5]$ and $N_{\mathrm{Rm}} \in [1.1, 2.3]$ for $\mathcal{M} = 0.1$, and $p_{\mathrm{Rm}} \in [1.2, 1.6]$ and $N_{\mathrm{Rm}} \in [0.1, 0.7]$ for $\mathcal{M} = 10$. The resulting magnetic Prandtl number ($\mathrm{Pm} = \mathrm{Rm}/\mathrm{Re}$) is consistent with a constant value of 1.3 ± 1.1 for $\mathcal{M} = 0.1$, and 2.0 ± 1.4 for $\mathcal{M} = 10$. We compare our results with an independent study in the subsonic regime and find excellent agreement in p_{Re} and p_{Rm}, and agreement within a factor of ~ 2 for N_{Re} and N_{Rm} (due to differences in the codes and solvers). We compare these results to the target Re and Rm set in direct numerical simulations (DNS, i.e., using explicit viscosity and resistivity) from the literature. This comparison and our ILES relations can be used to determine whether a target Re and Rm can be achieved in a DNS for a given N. We conclude that for the explicit (physical) dissipation to dominate over the numerical dissipation, the target Reynolds numbers must be set lower than the corresponding numerical values.

Key words: methods:numerical - viscosity - resistivity - turbulence - MHD - dynamo - magnetic fields

1 INTRODUCTION

Turbulence is a critical physical process, with relevance in weather prediction, climate models, the oceans (Gargett 1989; Sohail et al. 2019), in engines, industrial burners, and turbines (Giusti & Mastorakos 2019; Leggett et al. 2022), as well as in the aerospace (Park et al. 2022) and automotive industries (Igali et al. 2019). However, turbulence also plays a crucial role in astrophysical systems, especially in the interstellar medium of galaxies (Ferrière 2001; Elmegreen & Scalo 2004; Mac Low & Klessen 2004; McKee & Ostriker 2007; Hennebelle & Falgarone 2012), with particular relevance for star formation (Padoan et al. 2014; Federrath 2018).

Turbulence is intrinsically three-dimensional (3D) and complex, with non-linear interactions being a key to generating turbulent flows, which are impossible to tackle via analytic calculations. Thus, we rely on numerical solutions of the turbulent systems by solving the governing magneto-hydro-dynamical (MHD) equations on a set of particles or grid cells (e.g., Price & Federrath 2010), via discretisation of the continuous fluid equations.

Discretisation of the MHD equations in time (time-step) and space (grid-size) introduces second-order difference terms that have viscous-like effects, particularly in regions where strong gradients (shearing motions or shocks) are present. These numerical effects are often referred to as numerical viscosity and numerical resistivity, because their mode of operation is similar to that of physical viscosity and resistivity. The physical (explicit) terms may be included in numerical simulations (Laney 1998; Bodenheimer 2007; Schmidt & Federrath 2011; Waagan et al. 2011; Dumbser et al. 2019), however, the numerical (implicit) contributions to dissipation are always present as well.

Magnetic fields are an essential component in astrophysical systems over a wide range of scales spanning from planets (Stevenson 2003; Jones 2011; Kochukhov 2021) to stars (Federrath 2015; Sharda et al. 2021), galaxies (Ruzmaikin et al. 1988; Beck & Wielebinski 2013; Seta et al. 2021), accretion discs around black holes (Penna et al. 2010; Zamaninasab et al. 2014), and even the early Universe (Subramanian 2010; Sur et al. 2010). These magnetic fields are subject to interaction with the fluid motions, including reconnection events (Lazarian et al. 2020). Furthermore, magnetic fields can be amplified in turbulent systems by a mechanism called the 'turbulent dynamo', by converting turbulent kinetic energy to magnetic energy (Widrow 2002; Brandenburg & Subramanian 2005; Kulsrud & Zweibel 2008; Federrath 2016; Rincon 2019; Achikanath Chirakkara et al. 2021; Seta & Federrath 2020, 2022; Hew & Federrath 2023).

In turbulent fluids, energy transfers from large to small scales (Kolmogorov 1991a; Frisch 1995; Goto 2008). As the energy cascades to smaller scales, it eventually reaches a spatial scale where it is dis-

★ E-mail: lakshmimalva@iisc.ac.in
† E-mail: christoph.federrath@anu.edu.au

© 2023 The Authors

sipated due to the effects of viscosity and resistivity (Kolmogorov 1991b; Ertesvåg & Magnussen 2000). The Fourier wave numbers associated with these dissipation scales are called viscous dissipation wave number k_ν and resistive dissipation wave number k_η, respectively. The corresponding hydrodynamic Reynolds number (Re) is defined as

$$\mathrm{Re} = \frac{u_\mathrm{turb}\,\ell_\mathrm{turb}}{\nu}, \tag{1}$$

where u_turb is the fluid turbulent velocity dispersion at the turbulence driving scale $\ell_\mathrm{turb} = 2\pi/k_\mathrm{turb}$, with k_turb being the turbulence driving wave number, and ν is the kinematic viscosity of the fluid. Eq. (1) characterises the relative contribution of inertial forces to viscous forces in a fluid flow.

Similarly, the magnetic Reynolds number (Rm) is defined as

$$\mathrm{Rm} = \frac{u_\mathrm{turb}\,\ell_\mathrm{turb}}{\eta}, \tag{2}$$

where η is the magnetic resistivity. Eq. (2) represents the ratio between the induction forces and magnetic dissipation.

The magnetic Prandtl number (Pm), which controls the scale separation between k_ν and k_η, is given by

$$\mathrm{Pm} = \frac{\mathrm{Rm}}{\mathrm{Re}}. \tag{3}$$

Together, Re, Rm, and Pm, represent the main plasma parameters, crucially controlling the dynamics, structure, and evolution of magnetised turbulent flows, and thus, it is critical to know them.

The degree of numerical viscosity (ν_N) or resistivity (η_N) must be sufficiently lower than the chosen explicit viscosity (ν) or resistivity (η), i.e., $\nu > \nu_N$ and $\eta > \eta_N$, for a simulation to avoid excessive smearing of features or over-damping of the flow. Otherwise, the physical state of the system significantly deviates from the expectations set by explicit viscosity or resistivity (Thornber et al. 2007; Obergaulinger et al. 2009; Rembiasz et al. 2017). This implies that the associated numerical Reynolds numbers must be greater than the explicit Reynolds numbers.

The problem faced in numerical simulations is that the lower the grid resolution, the greater will be the effects of numerical dissipation. We know that the spatial scales $l_\nu = 2\pi/k_\nu$ and $l_\eta = 2\pi/k_\eta$, at which kinetic and magnetic dissipation occurs, are directly related to the corresponding dissipation terms (viscosity ν and resistivity η). Therefore, the lower the target viscosity, the greater the grid resolution required to resolve the spatial scale to capture the dissipation range of the turbulent fluid (Haugen et al. 2004a; Balsara et al. 2004; Schekochihin et al. 2005; Federrath et al. 2011b). One way to estimate the effects of numerical viscosity and resistivity of a simulation is to perform convergence tests. By running several simulations with increasing N, the resulting numerical ν_N and η_N are reduced until the target explicit $\nu_N < \nu$ and $\eta_N < \eta$. However, resolution studies are time-consuming and computationally costly.

Thus, even though the target (explicit) Reynolds number is set for a simulation, we have to ensure that the grid resolution of the simulation is sufficient to capture the dissipation range set by the explicit dissipation terms. If not, the effects of the numerical dissipation will dominate and the Reynolds number of the simulation will technically be the numerical Reynolds number and not the target Reynolds number. Therefore, it is critical to have an estimate of the numerical viscosity or resistivity corresponding to a particular grid resolution.

Therefore, in this study, we determine the Reynolds numbers and characteristic dissipation wave numbers associated with numerical viscosity and resistivity for a given linear grid resolution N, by studying their variations with N, and establishing empirical relations for ideal MHD simulations. This provides us with estimates of the numerical viscosity and resistivity for a given N, thereby verifying whether the target Reynolds numbers as per expectation can be achieved.

In Section 2, we introduce our simulation methods, suite of simulation models, and describe the formulations for fitting kinetic and magnetic spectra, to extract the dissipation scales. Section 3 presents the main results, including the time evolution of the simulations, the spatial structure of the gas and magnetic field, as well as the spectral analysis that allows us to extract the viscous and resistive dissipation scales. In Section 4, we convert the measured dissipation scales to their respective Reynolds numbers, and provide models for their dependence on the numerical grid resolution. In Section 5 we compare our results to a similar study that was limited to the subsonic regime of turbulence, and we set our results in the context of simulations in the literature that explicitly aim to control the Reynolds numbers. We summarise our results in Section 6.

2 METHODS

2.1 Simulations

2.1.1 Basic Equations

We consider the ideal, compressible magnetohydrodynamic equations (MHD) for isothermal plasma, given by

$$\frac{\partial \rho}{\partial t} + \nabla\cdot(\rho\mathbf{u}) = 0, \tag{4}$$

$$\rho\left(\frac{\partial}{\partial t} + \mathbf{u}\cdot\nabla\right)\mathbf{u} = \frac{1}{4\pi}(\mathbf{B}\cdot\nabla)\mathbf{B} - \nabla P_\mathrm{tot} + \nabla\cdot(2\nu\rho\mathbf{S}) + \rho\mathbf{F}, \tag{5}$$

$$\frac{\partial \mathbf{B}}{\partial t} = \nabla\times(\mathbf{u}\times\mathbf{B}) + \eta\nabla^2\mathbf{B}, \tag{6}$$

$$\nabla\cdot\mathbf{B} = 0, \tag{7}$$

where ν is the kinematic viscosity, η is the magnetic resistivity, ρ is the fluid density, $\mathbf{u}$ is the fluid velocity, $\mathbf{B}$ is the magnetic field, $P_\mathrm{tot} = P_\mathrm{th} + |\mathbf{B}|^2/(8\pi)$ is the total pressure, with the thermal pressure $P_\mathrm{th} = c_\mathrm{s}^2\rho$ (c_s is the constant speed of sound) and the magnetic pressure $|\mathbf{B}|^2/8\pi$, and $\mathbf{F}$ is the turbulent acceleration field (discussed in §2.1.2). The strain rate tensor $S_{ij} = (1/2)(\partial_i u_j + \partial_j u_i) + (2/3)\delta_{ij}\nabla\cdot\mathbf{u}$ in the momentum equation, Eq. (5), incorporates the viscous dissipation rate. The energy equation is not included because the fluid is isothermal.

In the ideal-MHD case, ν and η are set to zero in the equations above, i.e., the respective dissipation terms are not included. However, as discussed in the introduction, numerical dissipation is always present, because the system of equations is solved in a discretised way, i.e., here on a numerical grid with N^3 grid cells. These cells have a finite spacing, which gives rise to numerical viscosity and resistivity. However, the numerical dissipation in grid-based codes has a similar effect as to what is mathematically described by the physical dissipation terms in Eqs. (5) and (6), i.e., $\nabla\cdot(2\nu\rho\mathbf{S})$ and $\eta\nabla^2\mathbf{B}$, however, with effective values of ν and η that depend on N. Therefore, throughout our study, ν and η refer to the numerical viscosity and resistivity, respectively, unless otherwise stated.

We solve Eqs. (4)–(7) with a modified version of the FLASH code on a uniformly discretised, triply-periodic, 3D grid with a box size length of L, for 6 numerical resolutions (total number of grid cells N^3), with N = 72, 144, 288, 576, 1152 and 2304, by utilising the HLL5R, 5-wave, approximate Riemann solver (Bouchut et al. 2007, 2010; Waagan et al. 2011).

2.1.2 Turbulence Driving

To drive turbulence, we use the Ornstein-Uhlenbeck process (Eswaran & Pope 1988; Schmidt et al. 2006; Federrath et al. 2010) implemented in the publicly available `TurbGen` (Federrath et al. 2022) code, which generates the turbulent acceleration field $\mathbf{F}$ in Eq. (5).

The turbulence driving amplitude is a paraboloid in Fourier space (with wave number k), which peaks at $k = k_{\rm turb} = 2$, where we measure k in units of $k_{\rm box} = 2\pi/L$, and the amplitude is set to 0 for $k \leq 1$ and $k \geq 3$. The driving amplitudes are adjusted such that the desired sonic Mach number ($\mathcal{M} = u_{\rm turb}/c_{\rm s}$) is 0.1 for the subsonic regime and $\mathcal{M} = 10$ for the supersonic regime, respectively.

Here we use purely solenoidal (divergence-free) driving of the turbulence, as it is traditionally used for subsonic (incompressible) studies of turbulence, and we aim to compare to such studies later in §5. For consistency we use the same driving (solenoidal) for the supersonic set of simulations. We note that we do not expect that our results depend on the turbulence driving mode, and leave a possible investigation of this aspect to a future study.

2.1.3 Initial Conditions and Simulation Parameters

We describe the following physical quantities in dimensionless units, with $c_{\rm s} = 1$ and $\rho_0 = 1$, the latter being the initial uniform density. Thus, $\mathbf{u}$ is in units of $c_{\rm s}$, ρ is in units of ρ_0, $\mathbf{B}$ is in units of $c_{\rm s}\rho_0^{1/2}$, and the dissipation wave numbers k_ν and k_η are in units of $k_{\rm box}$. In fact, throughout the study, all wave numbers are reported in units of $k_{\rm box}$.

We initialise a turbulent magnetic field with zero net flux, i.e., without a mean field. The fluctuating magnetic field is generated with `TurbGen` (Federrath et al. 2022), in analogy to the turbulence driving field, i.e., with a parabolic Fourier amplitude spectrum over $1 \leq k \leq 3$ (as described in §2.1.2). We set the root-mean-squared magnetic field value to $B = 3.54491e-11$ and $B = 3.54491e-9$ for the $\mathcal{M} = 0.1$ and $\mathcal{M} = 10$ simulations, respectively. These values give an Alfvén Mach number (ratio of turbulent velocity to Alfvén speed) of $\mathcal{M}_{\rm A} = u_{\rm turb}/v_{\rm A} = 10^{10}$ for all simulations, based on $u_{\rm turb} = 0.1$ and 10 for the subsonic and supersonic simulations sets, respectively. The respective values of plasma beta are $\beta = P_{\rm th}/P_{\rm mag} = 6.5\times10^{22}$ for $\mathcal{M} = 0.1$ (subsonic regime) and 6.5×10^{18} for $\mathcal{M} = 10$ (supersonic regime). The resulting peak initial magnetic energy is $E_{\rm mag,0} = 5\times10^{-23}$ in the subsonic simulation set and $E_{\rm mag,0} = 5\times10^{-19}$ in the supersonic simulation set, which means that the magnetic field is initially extremely weak, such that we can observe turbulent dynamo amplification. We note that as long as the field is weak, the initial field strength and structure do not affect the properties of the magnetic field generated by the dynamo (Seta & Federrath 2020).

Apart from the distinction of the subsonic and supersonic regimes of turbulence, which we parameterise with $\mathcal{M} = 0.1$ and 10, respectively, our primary focus is on the effects of the numerical resolution N. Thus, we run simulations with $N = 72$, 144, 288, 576, 1152 and 2304, for the subsonic and supersonic simulation sets. Tab. 1 lists these simulations and the main analysis results, which we discuss in Sections 3 and 4.

2.2 Spectral Fitting

In order to determine the dissipation scales of the turbulence, we directly fit a functional form to the kinetic and magnetic energy spectra, where the dissipation scales are fit parameters. We consider the model for the kinetic spectrum as a function of wave number k, defined in Kriel et al. (2022),

$$P_{\rm kin}(k) = A_{\rm kin} k^{p_{\rm kin}} \exp\left(-\frac{k}{k_\nu}\right). \tag{8}$$

Similarly, the functional form of the magnetic spectrum in Kriel et al. (2022) is defined as

$$P_{\rm mag}(k) = A_{\rm mag} k^{p_{\rm mag}} K_0\left(\frac{k}{k_\eta}\right), \tag{9}$$

In these equations, $A_{\rm kin}$ and $A_{\rm mag}$ are amplitude coefficients, $p_{\rm kin}$ and $p_{\rm mag}$ are slopes of the power-law parts of the spectra, and k_ν and k_η are the characteristic wave numbers where the dissipation terms dominate in $P_{\rm kin}$ and $P_{\rm mag}$, respectively. The function $K_0(x)$ is the modified Bessel function of the second kind and order 0.

Here we extend the model by Kriel et al. (2022) for $P_{\rm kin}$ to include the bottleneck effect (Falkovich 1994; Schmidt et al. 2004; Verma & Donzis 2007). With an assumption of local energy transfer (Falkovich 1994), the bottleneck effect signifies the suppression of non-linear interactions by dissipative modes, which decreases the efficiency of the energy cascade around that scale, resulting in a pile-up of kinetic energy in this range. Therefore, we define the modified functional form of the kinetic spectrum, including the bottleneck effect, as

$$P_{\rm kin}(k) = A_{\rm kin}\left[\left(\frac{k}{k_{\rm bn}}\right)^{p_{\rm kin}} + \left(\frac{k}{k_{\rm bn}}\right)^{p_{\rm bn}}\right] \exp\left[-\left(\frac{k}{\tilde{k}_\nu}\right)^{p_\nu}\right]. \tag{10}$$

In this model, the wave number is scaled by the additional fit parameters $k_{\rm bn}$ and $p_{\rm bn}$, in order to account for the different extents and strengths of the observed bottleneck effect across different linear grid resolutions, studied below. Finally, we generalise the exponential dissipation term with the exponent p_ν, in order to account for a slower or faster exponential decay compared to Eq. (8), close to k_ν, which we observe in our numerical simulation results below.

Likewise, we modify the functional form of the magnetic spectra by adding the exponent p_η in the Bessel function to account for a potentially slower or faster decay around k_η compared to Eq. (9), and obtain

$$P_{\rm mag}(k) = A_{\rm mag} k^{p_{\rm mag}} K_0\left[\left(\frac{k}{\tilde{k}_\eta}\right)^{p_\eta}\right]. \tag{11}$$

The generalisations of the dissipation functions in the spectral models, i.e., the additions of p_ν and p_η as exponents in the dissipation terms, thereby account for different levels of sharpness or smoothness of the transitions from the inertial range into the dissipation range. In order to obtain the characteristic wave numbers equivalent to the results in Kriel et al. (2022), the effect of the generalisation has to be reversed. Therefore, the value of the viscous dissipation wave number for the kinetic energy spectrum is computed as

$$k_\nu = \tilde{k}_\nu^{1/p_\nu}, \tag{12}$$

such that k_ν represents a value comparable to the one measured in Kriel et al. (2022), where $p_\nu = 1$. Similarly, the resulting value of the resistive dissipation wave number for the magnetic energy spectrum is given by

$$k_\eta = \tilde{k}_\eta^{1/p_\eta}. \tag{13}$$

In order to fit these models to the simulation data, we first compute time-averaged spectra from the simulations, in the kinematic regime of the turbulent dynamo, i.e., when the turbulence is fully developed and the magnetic energy grows exponentially. This is achieved by

Table 1. Simulation parameters and main results.

		From $P_{\rm kin}$					From $P_{\rm mag}$			Derived				
N	Γ	$p_{\rm kin}$	$p_{\rm bn}$	p_ν	$k_{\rm bn}$	$\tilde{k}_\nu$	$p_{\rm mag}$	p_η	$\tilde{k}_\eta$	k_ν	k_η	Re	Pm	Rm
(1)	(2)	(3)	(4)	(5)	(6)	(7)	(8)	(9)	(10)	(11)	(12)	(13)	(14)	(15)
							$\mathcal{M} = 0.1$							
2304	5.2±0.4	-1.7	0.32±0.01	1.0	39.9±0.4	65.0±0.2	2.71±0.01	0.83±0.01	34.4±0.6	65.0±0.2	69.8±3.0	$1.4^{+0.2}_{-0.2}\times10^4$	$1.5^{+1.0}_{-0.5}$	$2.1^{+2.0}_{-0.7}\times10^4$
1152	3.3±0.1	-1.7	0.38±0.01	1.0	21.6±0.3	34.1±0.1	2.59±0.01	0.88±0.01	22.6±0.5	34.1±0.1	34.7±2.0	$6.0^{+1.0}_{-0.8}\times10^3$	$1.3^{+1.0}_{-0.5}$	$8.1^{+6.0}_{-3.0}\times10^3$
576	2.1±0.2	-1.7	0.42±0.02	1.0	11.5±0.2	18.1±0.1	2.56±0.02	0.89±0.01	12.8±0.4	18.1±0.1	17.5±1.0	$2.6^{+0.4}_{-0.3}\times10^3$	$1.2^{+0.9}_{-0.5}$	$3.1^{+2.0}_{-1.0}\times10^3$
288	1.3±0.1	-1.7	0.39±0.02	1.0	5.80±0.11	9.71±0.05	2.52±0.04	0.90±0.02	7.13±0.46	9.71±0.05	8.97±1.00	$1.1^{+0.2}_{-0.1}\times10^3$	$1.1^{+0.9}_{-0.4}$	$1.2^{+1.0}_{-0.4}\times10^3$
144	0.9±0.1	-1.7	0.30±0.03	1.0	2.35±0.11	5.34±0.04	2.82±0.10	0.79±0.03	2.39±0.40	5.34±0.04	3.04±0.78	$5.1^{+0.8}_{-0.7}\times10^2$	$0.41^{+0.4}_{-0.2}$	$2.1^{+2.0}_{-0.9}\times10^2$
72	0.5±0.1	-1.7	0.27±0.11	1.0	0.00±N/A	2.89±0.07	3.00±0.01	0.71±0.09	0.91±0.60	2.89±0.07	0.87±0.80	$2.2^{+0.4}_{-0.3}\times10^2$	$0.12^{+0.4}_{-0.1}$	$2.8^{+7.0}_{-3.0}\times10^1$
							$\mathcal{M} = 10$							
2304	0.8±0.2	-2.0	0.00±0.00	0.7	30.2±0.6	34.6±0.5	1.52±0.01	0.81±0.01	56.7±1.9	158.0±3.0	144.0±13.0	$1.8^{+0.3}_{-0.3}\times10^5$	$1.1^{+0.9}_{-0.4}$	$1.9^{+1.0}_{-0.7}\times10^5$
1152	0.7±0.1	-2.0	0.00±0.04	0.7	17.6±0.4	18.4±0.3	1.47±0.02	0.84±0.01	36.5±1.8	64.0±2.0	71.8±9.0	$4.6^{+0.9}_{-0.7}\times10^4$	$1.6^{+1.0}_{-0.7}$	$7.3^{+6.0}_{-3.0}\times10^4$
576	0.6±0.1	-2.0	0.00±0.04	0.7	10.5±0.3	9.89±0.24	1.43±0.03	0.86±0.02	22.9±1.7	26.4±0.9	37.8±6.6	$1.2^{+0.2}_{-0.2}\times10^4$	$2.6^{+2.0}_{-1.0}$	$3.2^{+2.0}_{-1.0}\times10^4$
288	0.5±0.1	-2.0	0.00±0.06	0.7	6.42±0.25	5.37±0.18	1.43±0.03	0.83±0.03	12.4±1.2	11.0±0.5	20.5±4.3	$3.3^{+0.7}_{-0.5}\times10^3$	$4.4^{+4.0}_{-2.0}$	$1.4^{+1.0}_{-0.6}\times10^4$
144	0.4±0.1	-2.0	0.00±0.02	0.7	4.01±0.23	2.95±0.14	1.52±0.05	0.75±0.03	5.23±0.70	4.68±0.33	8.98±2.30	$9.0^{+2.0}_{-2.0}\times10^2$	$4.7^{+5.0}_{-3.0}$	$4.2^{+4.0}_{-2.0}\times10^3$
72	0.5±0.1	-2.0	0.00±0.06	0.7	2.56±0.38	1.67±0.18	2.12±0.34	0.57±0.10	0.77±0.77	2.07±0.31	0.63±1.00	$2.7^{+0.8}_{-0.7}\times10^2$	$0.21^{+0.8}_{-0.2}$	$6.0^{+20.0}_{-5.0}\times10^1$

Note: All measured and derived parameters were obtained by time averaging over the kinematic (exponential growth) phase of the dynamo, from $t \geq 4t_{\rm turb}$ to when $E_{\rm mag}/E_{\rm kin} \leq 10^{-3}$, for both the subsonic ($\mathcal{M} = 0.1$) and supersonic ($\mathcal{M} = 10$) regimes (see §3.1.1). Columns: **(1)** Linear grid resolution N for our series of simulations. **(2)** The exponent of the time-rate of change Γ of $E_{\rm mag}/E_{\rm kin}$, i.e., the dynamo growth rate (see Eq. 14). The following columns are the measured parameters (fixed parameter values are shown without errors) from fitting Eq. (10) to $P_{\rm kin}$ from our numerical simulations. **(3)** Power-law exponent of the scaling range of $P_{\rm kin}$. **(4)** Exponent of the bottleneck effect of $P_{\rm kin}$. **(5)** Exponent of the dissipation term of $P_{\rm kin}$. **(6)** Scaling wave number of the bottleneck effect of $P_{\rm kin}$. **(7)** Viscous dissipation wave number if $p_\nu = 1$. The following columns are the measured parameters from fitting Eq. (11) to $P_{\rm mag}$. **(8)** Power-law exponent of the scaling range of $P_{\rm mag}$. **(9)** Exponent of the dissipation term of $P_{\rm mag}$. **(10)** Resistive dissipation wave number if $p_\eta = 1$. The following columns are the derived quantities from the previous columns. **(11)** Viscous dissipation wave number derived from column 7 (see Eq. 12). **(12)** Resistive dissipation wave number derived from column 10 (see Eq. 13). **(13)** Hydrodynamic Reynolds number derived from column 11 (see Eq. 15). **(14)** Magnetic Prandtl number derived from columns 11 and 12 (see Eq. 19). **(15)** Magnetic Reynolds number derived from columns 13 and 14 (see Eq. 3). The wave numbers are reported in units of $k_{\rm box}$ throughout the study (see §2.1.3). The error bars reported are two-sigma variations of the corresponding parameter.

time-averaging the power spectra from $t/t_{\rm turb} \geq 4$, to safely start when the turbulence is fully developed (Beattie et al. 2023) in both the subsonic and supersonic regime of turbulence. Moreover, the end of the time-averaging window is defined such that the ratio of magnetic energy ($E_{\rm mag} = |\mathbf{B}|^2/8\pi$) to kinetic energy ($E_{\rm kin} = \rho_0 u_{\rm turb}^2/2$) is $E_{\rm mag}/E_{\rm kin} \leq 10^{-3}$, in order to exclude the transition from the kinematic into the linear and saturated regimes of the dynamo.

Additionally, due to the growth of magnetic energy in the kinematic regime of the dynamo, in order to be able to time-average the magnetic energy, $P_{\rm mag}$ is first normalised by its total magnetic energy, which is the integral of $P_{\rm mag}(k)$ over all k, at each time frame. Thus, we effectively time-average the shape of $P_{\rm mag}(k)$ compensated by the amplitude increase over time, allowing for a robust measurement of k_η.

All spectra ($P_{\rm kin}$ and $P_{\rm mag}$) are fitted from $k \geq 3$ to only consider the range of fully-developed turbulence, excluding the turbulence driving scales. The upper limit of the fit in wave-number space is half the maximum k for every N, i.e., $k_{\rm max}/2 = N/4$. This is to exclude spurious numerical effects on scales smaller than 2 grid cell lengths.

For the kinetic spectra, $p_{\rm kin}$ is chosen to be $p_{\rm kin} = -1.7$ as per Kolmogorov's theory (Kolmogorov 1941, 1962; She & Leveque 1994; Federrath et al. 2021) for our subsonic set of simulations ($\mathcal{M} = 0.1$), and $p_{\rm kin} = -2.0$ as per Burgers turbulence (Burgers 1948; Bouchaud et al. 1995; Mac Low & Klessen 2004; Kritsuk et al. 2007; Federrath 2013; Federrath et al. 2021) for our set of supersonic simulations ($\mathcal{M} = 10$). While self-consistently fitting these exponents is possible for the highest-resolution simulation used here ($N = 2304$), it is practically impossible to do so for resolutions $N \lesssim 1000$ (Kitsionas et al. 2009; Federrath et al. 2010; Price & Federrath 2010; Kritsuk et al. 2011; Federrath 2013; Federrath et al. 2021). Thus, we fix these scaling exponents to allow for a robust determination of the dissipation wavenumbers.

The viscous dissipation exponent p_ν is fixed at 1.0 and 0.7 for the $\mathcal{M} = 0.1$ and 10 simulation sets, respectively. We fix these values to prohibit variations in this parameter for different numerical resolutions N, therefore preventing systematic dependencies on p_ν, while still providing excellent fits in both the subsonic and supersonic regimes of turbulence (see Appendix A).

The dissipation wave numbers k_ν and k_η, along with their errors, are extracted from weighted fits of $P_{\rm kin}$ and $P_{\rm mag}$, respectively, taking into account the one-sigma time variations at each k.

3 RESULTS

In this section, we aim to measure the effects of the magnetic energy amplification mechanism and the dissipation effects on the time-averaged kinetic and magnetic power spectra. We are particularly interested in their dependence on the linear grid resolution N. We always distinguish between the subsonic and supersonic regimes of turbulence. We begin by developing a qualitative understanding of the implications of the grid resolution by studying the morphology of the gas density, and the kinetic and magnetic energies. We then determine the dissipation wavenumbers from fits to the kinetic (P_{kin}) and magnetic (P_{mag}) power spectra across different N.

3.1 Time evolution

We start by explaining our choice of the time-averaging window of the power spectra as described in §2.2, by analysing the time frames corresponding to the different phases of our simulations represented in Fig. 1. Fig. 1 shows the time evolution of the sonic Mach number ($\mathcal{M}$) in the top two panels, and the ratio of magnetic to kinetic energy ($E_{\mathrm{mag}}/E_{\mathrm{kin}}$) in the bottom panels, for a series of linear grid resolutions (N) obtained from our numerical simulations in the subsonic ($\mathcal{M} = 0.1$; left panels) and supersonic ($\mathcal{M} = 10$; right panels) regimes.

In the early stages of a turbulent dynamo, called the kinematic phase, the fluid motion induces the stretching, twisting, folding, and merging of the magnetic field lines, leading to the amplification of the magnetic field (Brandenburg & Subramanian 2005; Schekochihin et al. 2004a; Federrath 2016). As the magnetic field grows, it begins to influence the fluid motion by exerting magnetic forces (Lorentz force) on the fluid. These magnetic forces modify the turbulent motions, ultimately leading to saturation of the dynamo. During the saturation phase, the magnetic field reaches a level where the energy gained from the turbulent motions is balanced by the energy dissipated through various processes, such as dissipation and diffusion. Therefore, the back-reaction of the magnetic fields through the Lorentz force is significant enough to suppress further amplification of the magnetic field.

3.1.1 *Defining the time-averaging window for spectral analysis*

The region of fully-developed turbulence in the time evolution plots of the sonic Mach numbers is the region after the transition from the initial transient rise to the state where the time-variations in $\mathcal{M}$ for all our simulations lie within 10–20% of our target $\mathcal{M}$, in both the subsonic and supersonic regimes. For the time evolution of $E_{\mathrm{mag}}/E_{\mathrm{kin}}$, the region prior to fully-developed turbulence, referred to as the initial transient phase, is signified by the irregularities in $E_{\mathrm{mag}}/E_{\mathrm{kin}}$ before the transition to the kinematic phase of the dynamo. We observe from the time evolution of $E_{\mathrm{mag}}/E_{\mathrm{kin}}$ that the kinematic phase starts at $t \approx 4t_{\mathrm{turb}}$ in both the subsonic and supersonic regimes (indicated by vertical dashed lines in Fig. 1).

We emphasise that most of our simulations do not reach the saturation phase of the dynamo. The transition from the kinematic to the linear phase can only be observed in the subsonic regime for the top three resolutions in our series of simulations. For all other models, in particular the supersonic runs, it is evident that the magnetic field continues to grow beyond $t/t_{\mathrm{turb}} = 20$ (the time at which we choose to stop the simulations due to computational costs, and the fact that this study focuses on the dissipation scales in the kinematic regime of the dynamo). Hence, the region below the horizontal line at $E_{\mathrm{mag}}/E_{\mathrm{kin}} = 10^{-3}$ and right of the vertical line at $t/t_{\mathrm{turb}} = 4$ marks the kinematic phase of the dynamo, safely away from the initial transient phase and the saturation phase, as shown in the bottom panels. Thus, this defines our time-averaging window for the spectral analysis below.

3.1.2 *Basic time evolution*

We start by comparing the magnetic amplification in the kinematic phase of the dynamo in the subsonic and supersonic regimes and for different numerical grid resolutions N. In order to do so, we fit an exponential model to $E_{\mathrm{mag}}/E_{\mathrm{kin}}$ in the time-averaging window (see §3.1.1), to quantify its time-rate of growth,

$$E_{\mathrm{mag}}/E_{\mathrm{kin}} = (E_{\mathrm{mag}}/E_{\mathrm{kin}})_0 e^{\Gamma(t-4)}, \tag{14}$$

where $(E_{\mathrm{mag}}/E_{\mathrm{kin}})_0$ is the value of $E_{\mathrm{mag}}/E_{\mathrm{kin}}$ at $t = 4t_{\mathrm{turb}}$. Γ, measured in units of t_{turb}^{-1}, quantifies the growth rate of $E_{\mathrm{mag}}/E_{\mathrm{kin}}$. The extracted Γ from the fit is listed in column 2 of Tab. 1. We observe that the growth rate of $E_{\mathrm{mag}}/E_{\mathrm{kin}}$ increases with N. We expect this because higher grid resolutions better capture magnetic field amplification by vorticity, which is dominant in smaller-scale turbulent motions of the fluid elements (Federrath et al. 2011a; Seta & Federrath 2020; Achikanath Chirakkara et al. 2021). Comparing the growth rates between the subsonic and supersonic regimes for a particular grid resolution, we find that the magnetic field amplification is higher for $\mathcal{M} = 0.1$ than for $\mathcal{M} = 10$ as in previous studies (Federrath et al. 2011a; Seta & Federrath 2020; Achikanath Chirakkara et al. 2021).

For the resolutions 2304, 1152 and 576 in subsonic simulations, we also observe a drop in the sonic Mach numbers due to the back-reaction on the fluid from the amplified magnetic field B in the region where $E_{\mathrm{mag}}/E_{\mathrm{kin}} \sim 10^{-1}$. This back-reaction on the velocity field is negligible in the kinematic phase of the dynamo, because the corresponding magnetic field is very weak.

3.2 Kinetic and Magnetic Energy Structure

Before going into the details of the spectral fitting analysis to determine the dissipation scales k_ν and k_η, we first look at some of the spatial features of our simulation sets, in order to get a qualitative sense of the effect of the numerical resolution N. Figs. 2 and 3 show two-dimensional projections from our simulations, of the fluid density (top panels), kinetic energy (E_{kin}; middle panels), and magnetic energy ($E_{\mathrm{mag}}/E_{\mathrm{mag},0}$; bottom panels), for the $\mathcal{M} = 0.1$ and $\mathcal{M} = 10$ simulation sets, respectively. The values on the colour bar are the spatial average through the entire line of sight along the z-axis of the simulation domain and at $t = 10t_{\mathrm{turb}}$, which lies in the kinematic phase of the dynamo. The lines in E_{kin} and $E_{\mathrm{mag}}/E_{\mathrm{mag},0}$ represent the streamlines of the velocity field and magnetic field, respectively. The panels from left to right correspond to 3 of our 6 grid resolutions, here for $N = 72$, 288, and 1152.

In the subsonic regime, the density variations are only of the order of 1% from minimum to maximum density. In contrast to this, we see very large (order-of-magnitude) density variations in the supersonic simulation sets, shown in the top panels of Fig. 3, as expected from the shock-jump condition $d\rho \sim \mathcal{M}^2$. It is also evident how smaller-scale variations in the density are better resolved at higher numerical resolution.

The kinetic energy does not display a strong resolution dependence, because the kinetic energy is dominated by contributions of large-scale eddies, which implies that E_{kin} has converged on relatively larger spatial scales, which is indeed what we see in the middle panels of Figs. 2 and 3.

In contrast to the structure of E_{kin}, the scale of the magnetic field lines (bottom panels) decreases with increasing resolution. This is because magnetic amplification due to vorticity (deformations of the magnetic field lines by local stretching, twisting and folding of fluid elements) is driven by the turbulent eddies on relatively smaller spatial scales. Therefore, with an increase in grid resolution, smaller-

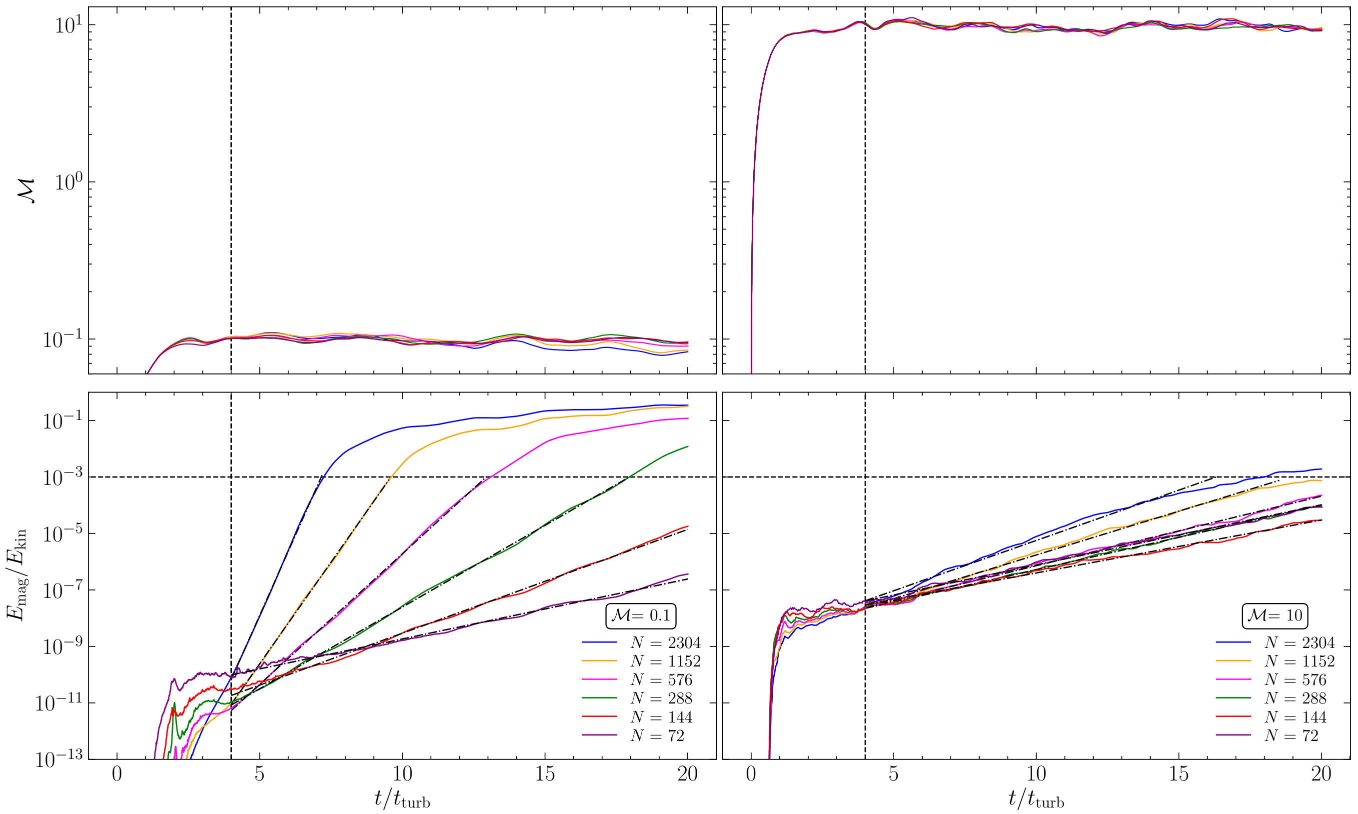

Figure 1. Time evolution of the sonic Mach number ($\mathcal{M}$; top panels), and the ratio of magnetic to kinetic energy ($E_{\rm mag}/E_{\rm kin}$; bottom panels). The left panels show our set of subsonic simulation models ($\mathcal{M} = 0.1$) and the right panels show our set of supersonic simulation models ($\mathcal{M} = 10$). After the initial transient phase, $t \lesssim 4t_{\rm turb}$, (marked by the vertical lines), the turbulence in all our simulations is fully developed and the magnetic field has entered the exponential (kinematic) growth phase of the turbulent dynamo. $E_{\rm mag}/E_{\rm kin} = 10^{-3}$ (marked by the horizontal lines in the bottom panels) safely separates the kinematic phase of the dynamo from the linear (and saturated) phase of the dynamo, for all simulations in our series of N. Therefore, we only consider times $t \geq 4t_{\rm turb}$ and when $E_{\rm mag}/E_{\rm kin} \leq 10^{-3}$ for time-averaging the power spectra (c.f., §2.2). The growth rate of $E_{\rm mag}/E_{\rm kin}$ (marked by black dashed lines overlaid in the bottom panels) is obtained from fitting Eq. (14) in the kinematic phase of the dynamo, and is listed in column 2 of Tab. 1.

scale vortices are captured to a greater extent, causing an increase in $E_{\rm mag}$. For the $\mathcal{M} = 10$ case, regions of higher magnetic and kinetic fields are correlated with high-density regions. This suggests the occurrence of magnetic energy amplification due to the process of shock creation (rapid compression of fluid elements), which primarily occurs on relatively larger scales compared to vorticity, in the supersonic regime. However, as we shall show later, the dominant mechanism for magnetic energy amplification in both subsonic and supersonic regimes is due to vorticity (see Appendix B). This suggests the small-scale eddies live inside the large-scale shocks created.

3.3 Kinetic and Magnetic Power Spectra

Fig. 4 shows the time-averaged kinetic power spectra ($P_{\rm kin}$; top panels), and magnetic power spectra ($P_{\rm mag}$; bottom panels), plotted against wave number k, along with their error bars (time variations from the time-averaged power for a particular k), for the series of N, obtained from our simulations. The left panels belong to the subsonic regime and the right panels belong to the supersonic regime. Eqs. (10) and (11) are fitted to $P_{\rm kin}$ and $P_{\rm mag}$ (taking into account the one-sigma time variations at each k), respectively, in the kinematic regime of the dynamo as described in §2.2. Except for the highest resolution ($N = 2304$), each power spectrum and its corresponding fit are multiplied by 0.1 relative to its nearest higher resolution case for ease of visualisation, i.e., to allow for a visual separation of the curves. The extracted dissipation wave numbers from $P_{\rm kin}$ and $P_{\rm mag}$ (k_ν and k_η, respectively) are displayed as tick markers on the wave-number axis, with colour code according to that of the power spectra.

We see that the spectrum models given by Eqs. (10) and (11) fit $P_{\rm kin}$ and $P_{\rm mag}$ well within their error bars. The fit parameters obtained from spectral fitting are listed in Tab. 1. The parameter errors listed in the table are the two-sigma errors. We emphasise that we have only fitted data within the range $3 \leq k \leq k_{\rm max}/2$ for each resolution, to safely exclude the low-k turbulence driving range, and the slight upturn observed at high k, which is caused by numerical effects (note that limiting the fit to $k \leq k_{\rm max}/2$ means that we exclude data on the scale of a couple of grid cells).

We now comment on the fit model parameters.

3.3.1 *Kinetic power spectra ($P_{\rm kin}$)*

3.3.1.1 Power-law scaling exponent $p_{\rm kin}$. $p_{\rm kin}$ is the power-law exponent of the self-similar scaling range of the turbulence. We note that measuring $p_{\rm kin}$ requires very high resolution N. For $N = 2304$, we find exponents of $p_{\rm kin} \sim -1.7$ and $p_{\rm kin} \sim -2.0$ for the subsonic and supersonic regimes, respectively. However, we cannot determine $p_{\rm kin}$ self-consistently for the low-resolution models. Thus, we fix $p_{\rm kin}$ to the the values determined for the highest-resolution sets, and consistent with the theoretical expectations for $p_{\rm kin} \sim -1.7$ in

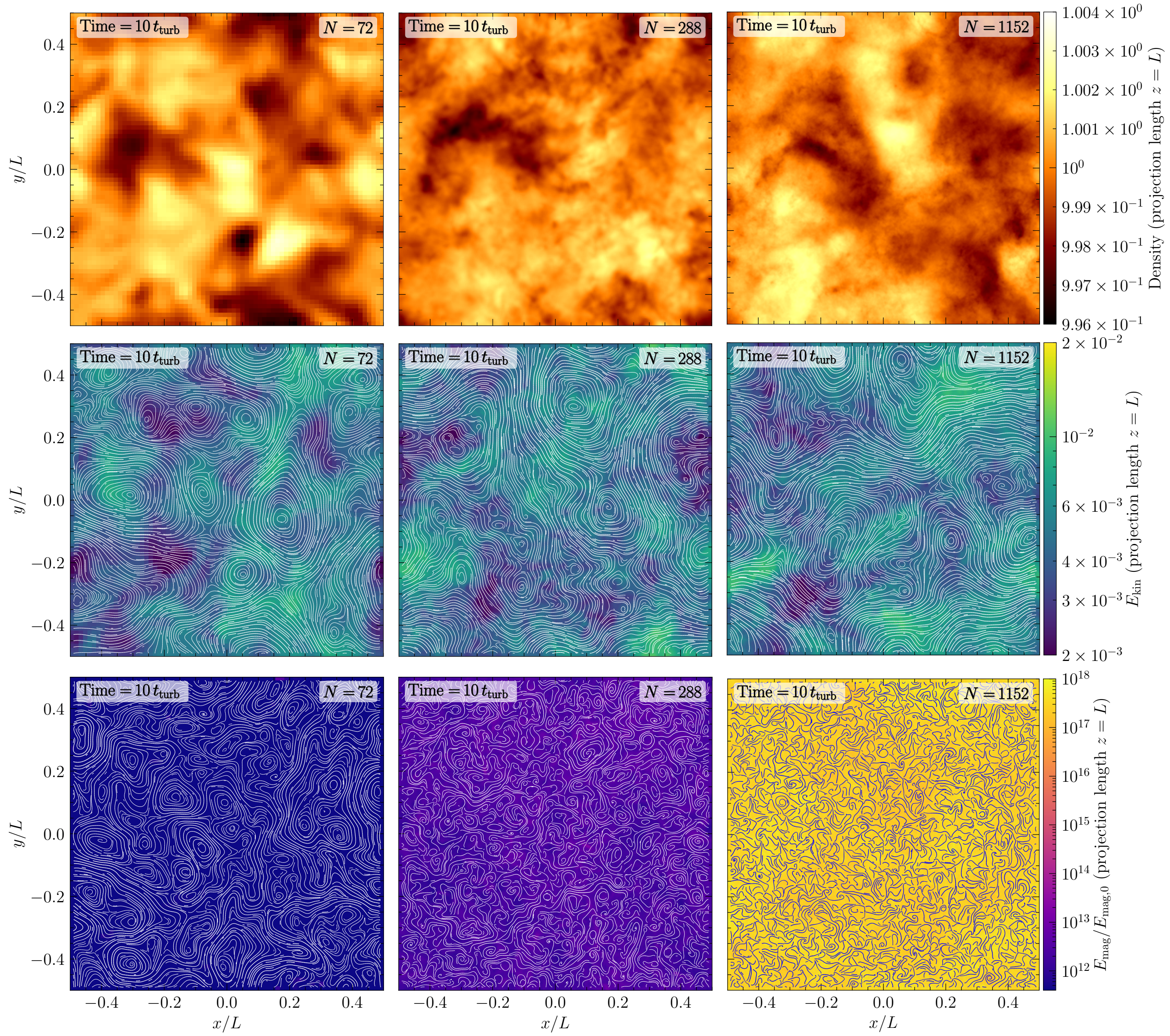

Figure 2. Two-dimensional projections (spatial average along the entire z-axis), in the subsonic regime ($\mathcal{M} = 0.1$) of fluid density (top panels), kinetic energy ($E_{\rm kin}$; middle panels), and magnetic energy ($E_{\rm mag}/E_{\rm mag,0}$; bottom panels) in the kinematic phase of the dynamo at $t = 10t_{\rm turb}$. Left to right panels correspond to 3 of our 6 grid resolutions (N), with the leftmost, middle, and rightmost panels showing $N = 72$, 288, and 1152, respectively. **(i) Top panels:** The density variations are of the order of 1% as expected for $\mathcal{M} \sim 0.1$. **(ii) Middle panels:** Large-scale eddies dominate the kinetic energy, and hence, $E_{\rm kin}$ does not show a significant resolution dependence. **(iii) Bottom panels:** Vorticity, predominant in the smallest-scale eddies, is principally responsible for the exponential magnetic field amplification in the subsonic regime. We see that increasing N leads to resolving smaller-scale magnetic field loops.

the subsonic regime (Kida & Murakami 1987; Sanada 1992; She & Leveque 1994; Smith & Reynolds 1991; Federrath et al. 2021), and $p_{\rm kin} \sim -2.0$ in the supersonic regime (Kritsuk et al. 2007; Federrath et al. 2010; Federrath 2013; Federrath et al. 2021).

3.3.1.2 Bottleneck exponent ($p_{\rm bn}$). We find that the bottleneck effect is more pronounced in the subsonic regime than in the supersonic regime, which is reflected in the higher values of $p_{\rm bn}$ for $\mathcal{M} = 0.1$ compared to $\mathcal{M} = 10$. Indeed, we find that $p_{\rm bn} \sim 0$ in the supersonic regime. In the subsonic regime, we find $p_{\rm bn} \sim 0.27$–0.42, without a systematic dependence on N.

3.3.1.3 Sharpness of viscous dissipation transition (p_ν). Concerning the sharpness of the transition from the power-law scaling range into the dissipation range (modelled with p_ν), we find that it is somewhat softer (extending over a somewhat larger range of scales) for $\mathcal{M} = 10$ compared to $\mathcal{M} = 0.1$. Therefore, we choose $p_\nu = 0.7$ for $\mathcal{M} = 10$, compared to $p_\nu = 1.0$ for $\mathcal{M} = 0.1$, which provide very good fits of the transition, for all N.

3.3.1.4 Bottleneck and viscous dissipation scales ($k_{\rm bn}$ and k_ν). We find that $k_{\rm bn}$ and k_ν (determined from $\tilde{k}_\nu$ via Eq. 12) increase systematically with N, in both the subsonic and supersonic regimes. From Tab. 1, we see that as N increases by a factor of 2, $k_{\rm bn}$ and k_ν

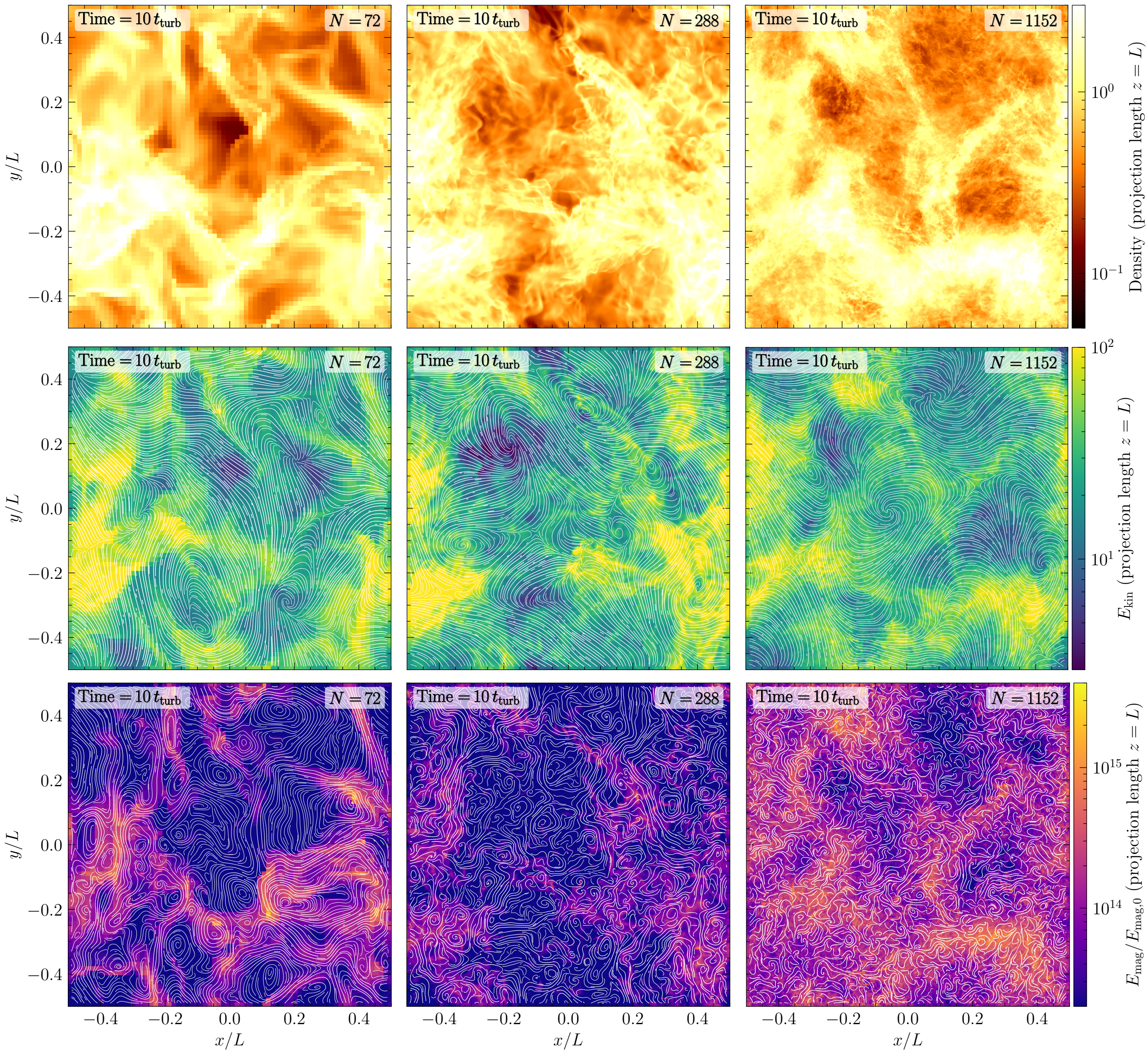

Figure 3. Same as Fig. 2, but for the supersonic ($\mathcal{M}$ = 10) simulations. **(i) Top panels:** In contrast to the subsonic simulations, here the density variations occupy several orders of magnitude as expected for supersonic turbulence. **(ii) Middle panels:** Similar to the subsonic regime, $E_{\rm kin}$ does not show a significant resolution dependence due to the dominant contribution of large-scale eddies and shocks. **(iii) Bottom panels:** The process of shock production due to the compression of fluid elements, which primarily happens on considerably larger scales (length of shocks) than vorticity, is prominently occurring in the supersonic regime. The shocks modify the structure of the magnetic field and vorticity production (primarily reducing it compared to the subsonic regime Federrath et al. 2011a). Due to the presence of shocks, we expect $P_{\rm mag}$ to be higher for small k in $\mathcal{M}$ = 10 compared to $\mathcal{M}$ = 0.1. For the same reason, regions of high magnitude of magnetic and kinetic fields correspond to regions of relatively higher density. The greater resolution of magnetic field scales with N and the associated exponential amplification implies that the turbulent dynamo still operates via stretch-twist-fold-merge and vorticity, even in the presence of shocks.

approximately double for $\mathcal{M}$ = 0.1, and they increase by a factor of $\sim$ 2.5 for $\mathcal{M}$ = 10. Therefore, we expect k_ν to vary approximately linearly with N, at least in the subsonic regime. However, we will quantify this in detail below (see §4.1). We also note that $k_{\rm bn} \lesssim 20$ for $N \lesssim 1000$, which means that the bottleneck (and the transition into dissipation) starts on relatively large scales for low N, reflecting the challenges in measuring $p_{\rm kin}$ for low N. In other words, there is practically no scaling range over which $p_{\rm kin}$ can be reliably measured if $N \lesssim 1000$ (Kritsuk et al. 2007; Kitsionas et al. 2009; Federrath et al. 2010; Price & Federrath 2010; Federrath 2013; Federrath et al. 2021).

3.3.2 *Magnetic power spectra ($P_{\rm mag}$)*

We now turn our attention to the magnetic power spectra in the bottom panels of Fig. 4, in order to understand the properties of k_η. We find that $P_{\rm mag}$ is higher for small wave numbers in the supersonic regime compared to the subsonic regime, for all grid resolutions. This signifies the role of shocks compressing the magnetic field, which

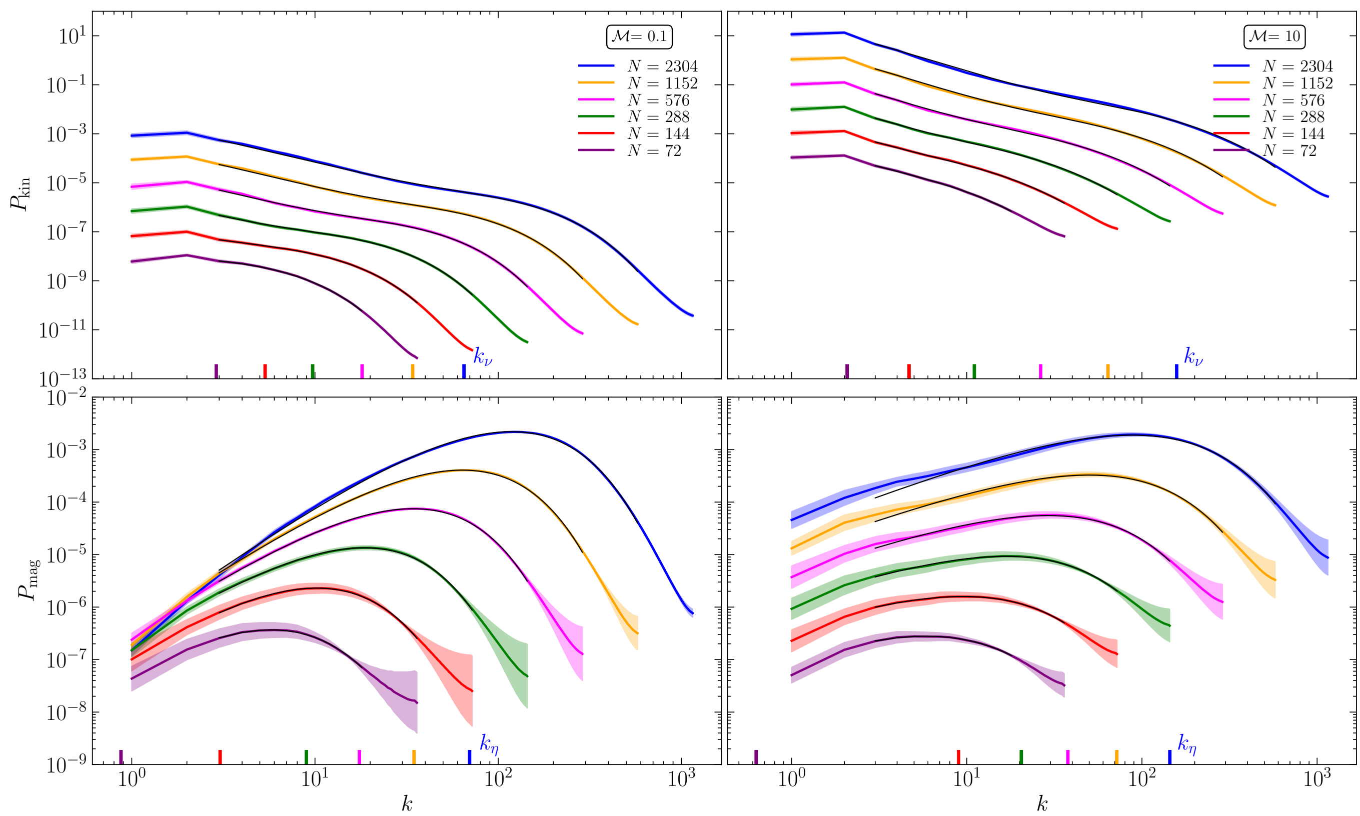

Figure 4. Time-averaged kinetic power spectra ($P_{\rm kin}$; top panels) and magnetic power spectra ($P_{\rm mag}$; bottom panels) for the series of linear grid resolutions N (see legend). The left panels are for $\mathcal{M} = 0.1$ and the right panels are for $\mathcal{M} = 10$. $P_{\rm kin}$ and $P_{\rm mag}$ for every N except $N = 2304$ is multiplied by a factor of 0.1 relative to the next-higher resolution. We overplot our fitted spectrum models (Eqs. 10 and 11) as thin black lines. Tab. 1 lists the fit parameters with columns 11 and 12 for the viscous dissipation wave number k_ν and the resistive dissipation wave number k_η, respectively, shown as coloured tick markers on the k-axis, in units of $k_{\rm box}$, corresponding to the colour code of the power spectra.

have relatively large length scales (overall size of the shocks, as opposed to their width). However, we note that the magnetic field is amplified also at larger k in the supersonic regime, which implies the existence of magnetic field amplification due to the turbulent dynamo and the role of vorticity, taking place on smaller spatial scales. Moreover, shocks are very thin and can compress the field to small scales inside shocks. A more quantitative discussion of these effects is needed in future studies comparing subsonic and supersonic turbulence (Kriel et al. 2023), while here we focus on measuring the dissipation scales.

3.3.2.1 Power-law scaling exponent $p_{\rm mag}$. We find $p_{\rm mag} \sim 2.7$–3.0 for $\mathcal{M} = 0.1$ and $p_{\rm mag} \sim 1.5$–2.1 for $\mathcal{M} = 10$, with slight variations with N. Based on Kazantsev et al. (1985), one theoretically expects $p_{\rm mag} = 3/2$ for the turbulent dynamo. However, due to limited resolution, we may not be able to find this theoretical value. It is also possible that the theoretical model for $p_{\rm mag}$ does not fully describe the physical system, and may not apply equally in the subsonic and supersonic regimes. Due to these caveats, we allowed this parameter to vary and fitted it (instead of fixing it as for $p_{\rm kin}$). While we caution numerical-resolution effects on $p_{\rm mag}$, we find significant differences in $p_{\rm mag}$ between the subsonic and supersonic regimes of turbulence, which may be a consequence of the presence of shocks, leading to more magnetic power on larger scales as compared to the subsonic regime. A dedicated study with extremely high resolution is needed to determine the physically converged value of $p_{\rm mag}$ in the subsonic and supersonic regimes of the turbulent dynamo.

3.3.2.2 Sharpness of resisitive dissipation transition p_η. We find relatively robust values of p_η, with $p_\eta \sim 0.6$–0.9 for both the subsonic and supersonic regimes, with only a weak dependence on N. Thus, since $p_\eta \lesssim 1$, the transition is somewhat smoother than for $p_{\rm mag} = 1$, but only very mildly so.

3.3.2.3 Resistive dissipation scale (k_η). First, the resistive dissipation wave number (k_η) is determined from $\tilde{k}_\eta$ via Eq. (13) as discussed in Sec. 2.2. We find that the onset of the dissipation range of $P_{\rm mag}$ for a particular N takes place at a larger k in the supersonic regime compared to the subsonic regime, with k_η about twice as large for $\mathcal{M} = 10$ compared to $\mathcal{M} = 0.1$. For a particular sonic Mach number, k_η approximately doubles as N increases by a factor of 2. Therefore, we expect k_η to vary linearly with N, as we will quantify in detail below.

4 EFFECTIVE REYNOLDS NUMBERS (Re, Rm) IN IDEAL MHD

Our main goal here is to determine the dissipation properties of grid-based ideal MHD turbulence simulations as a function of the grid resolution N. We do so in two layers. We first determine the variations of the viscous dissipation wave number (k_ν) and the resistive dissipation wave number (k_η) with N, which are the scales at which kinetic and magnetic energy begin to dissipate, respectively. Using the relations established in Kriel et al. (2022), we calculate the hydrodynamic Reynolds number (Re) and the magnetic Reynolds number (Rm) as a function of N.

4.1 Dependence of dissipation wave numbers, k_ν and k_η, on N

4.1.1 Formulation and Results

We start by developing models for k_ν and k_η as a function of N. As discussed previously in §3.3, we expect k_ν and k_η to vary linearly with N.

We consider the following relation between k_ν and Re from Kriel et al. (2022),

$$k_\nu = c_\nu k_{\mathrm{turb}} \mathrm{Re}^{1/p_{\mathrm{Re_{theo}}}}, \tag{15}$$

with the coefficient $c_\nu = 0.025^{+0.005}_{-0.006}$ determined in Kriel et al. (2022), and the theoretical scaling exponents $p_{\mathrm{Re_{theo}}} = 4/3$ in the subsonic regime ($\mathcal{M} = 0.1$) (Kolmogorov 1991a; Frisch 1995; Kriel et al. 2022) and $p_{\mathrm{Re_{theo}}} = 3/2$ in the supersonic regime ($\mathcal{M} = 10$)[1]. This implies a relation between Re and N, postulated as

$$\mathrm{Re} = \left(\frac{N}{N_{\mathrm{Re}}}\right)^{p_{\mathrm{Re}}}, \tag{16}$$

where N_{Re} is the grid resolution at which $\mathrm{Re} = 1$, i.e., occurring at the Kolmogorov micro-scale, and p_{Re} is the power-law exponent in that relation. Theoretically, we expect $p_{\mathrm{Re}} = p_{\mathrm{Re_{theo}}}$, but we will measure p_{Re} directly from the simulations. We note that $p_{\mathrm{Re}} = p_{\mathrm{Re_{theo}}}$ is required for k_ν to depend linearly on N.

The relation for k_ν on N is the resulting model obtained from plugging Eq. (16) into Eq. (15), which results in

$$k_\nu = c_\nu k_{\mathrm{turb}} \left(\frac{N}{N_{\mathrm{Re}}}\right)^{p_{\mathrm{Re}}/p_{\mathrm{Re_{theo}}}}. \tag{17}$$

In order to determine the values of p_{Re} and N_{Re}, we fit Eq. (17) to k_ν obtained from the simulations' power spectra as a function of N, with 2-sigma variations taking into account during fitting (see column 11 in Tab. 1). The resulting plot is shown in the top panels of Fig. 5, with the left and right panels for the subsonic and supersonic regimes, respectively. The fit parameter values obtained are presented in the figure legends, with an error of N/A indicating that the corresponding parameter was maintained fixed for the associated fit. We discuss the behaviour of the fit parameters in §4.1.2.

A clear and robust result from these simulations is that we find that k_η varies linearly with N in both the subsonic and supersonic regimes of turbulence. We note that the lowest-resolution cases ($N = 72$ and 144) are the only simulations that show some deviations from this, which is expected, given that those models are extremely low in resolution.

Therefore, we analyse the dependence of the resistive dissipation wave number on grid resolution by fitting the linear relation,

$$k_\eta = c_{\mathrm{lin}} N, \tag{18}$$

to k_η obtained from the simulations (with 2-sigma variations taken into account; see column 12 in Tab. 1), and c_{lin} is displayed in the legend in the bottom panels of Fig. 5.

[1] The exponent $p_{\mathrm{Re_{theo}}} = 3/2$, since $\mathrm{Re} \propto u(\ell)\ell \propto \ell^{3/2} \propto N^{3/2}$ (see Eq. 1), because $u(\ell) \propto \ell^{1/2}$ in the supersonic regime (Federrath 2013; Federrath et al. 2021).

In order to link this linear relation to the commonly established relation for k_η in the literature, we now consider the following relation (Kriel et al. 2022):

$$k_\eta = c_\eta k_\nu \mathrm{Pm}^{1/2}, \tag{19}$$

with the coefficient $c_\eta = 0.88^{+0.21}_{-0.23}$ measured in Kriel et al. (2022).

We propose the following model for Rm as a function of N, in analogy to Eq. (16), i.e., Rm is defined identically to Re, with the only difference being the use of resistivity instead of viscosity in the denominator (c.f., Eqs. 1 and 2),

$$\mathrm{Rm} = \left(\frac{N}{N_{\mathrm{Rm}}}\right)^{p_{\mathrm{Rm}}}. \tag{20}$$

The resulting formulation for the relation between k_η and N obtained by substituting Eqs. (20), (15) and (16) into Eq. (19), is

$$k_\eta = c_\nu c_\eta k_{\mathrm{turb}} \frac{N^{p_{\mathrm{Re}}/p_{\mathrm{Re_{theo}}} - p_{\mathrm{Re}}/2 + p_{\mathrm{Rm}}/2}}{N_{\mathrm{Re}}^{p_{\mathrm{Re}}/p_{\mathrm{Re_{theo}}} - p_{\mathrm{Re}}/2}\, N_{\mathrm{Rm}}^{p_{\mathrm{Rm}}/2}}. \tag{21}$$

We fit Eq. (21) to k_η, and extract p_{Rm} and N_{Rm}. The resulting plot is shown in the bottom panels of Fig. 5. We discuss the characteristics of k_η as a function of N in §4.1.2.

4.1.2 Discussion

In this section, we aim to understand the effects of linear grid resolution N on the dissipation scales. Hence, we study the properties of the dependence of the dissipation wave numbers k_ν and k_η on N. Before that, we reason out the reliability of the simulation results based on their numerical resolution. Columns 13 and 14 of Tab. 1 list Re and Pm calculated from k_ν and k_η obtained from the power spectra (columns 11 and 12) using Eqs. (15) and (19), respectively. The Rm (column 15) is calculated from the resulting Re and Pm using Eq. (3). For magnetic amplification to dominate over magnetic dissipation in the kinematic phase of the dynamo, Rm has to exceed a critical value of $\mathrm{Rm_{crit}} \simeq 100$, depending on the sonic Mach number and Pm of the fluid (Schekochihin et al. 2004a,b; Haugen & Brandenburg 2004; Brandenburg & Subramanian 2005; Schober et al. 2012; Federrath et al. 2014; Achikanath Chirakkara et al. 2021). We find that $\mathrm{Rm} \gtrsim 100$ for $N \gtrsim 100$. We also know that, generally, turbulence fully develops for $\mathrm{Re} \gtrsim 100$–1000 (Frisch 1995; Schumacher et al. 2014), although it depends on the geometry of the system. We find that $\mathrm{Re} < 1000$ for $N = 72$ and 144, for both $\mathcal{M} = 0.1$ and 10, while $\mathrm{Re} \gtrsim 1000$ for $N \gtrsim 200$–300. This implies that fluid motions for the lowest two resolutions are borderline turbulent, and the intensity of turbulence, characterised by Re, increases with N. Therefore, the two lowest-resolution runs ($N = 72$ and 144) are expected to show deviations from the scaling relations that we establish in this work. Indeed, we see in Fig. 5 that these two resolutions show some deviations from the power-law scaling relations with N (especially for $N = 72$), in particular for k_η (bottom panels).

The dotted lines in Fig. 5 represent the basic theoretical relations for k_ν and k_η, i.e., the formulated models plotted with fixed parameters given by theory, as displayed. The dashed lines are fits of the dissipation wave numbers with at least one (but not all) parameter left free to vary, and the solid lines are fitted with all the parameters left free to vary.

4.1.2.1 Viscous dissipation scale (k_ν): We start by discussing the dependence of the viscous dissipation wave number k_ν on the grid resolution N. We note that (see Appendix D)

$$p_{\mathrm{Re}} = \frac{1 - p_{\mathrm{kin}}}{2}. \tag{22}$$

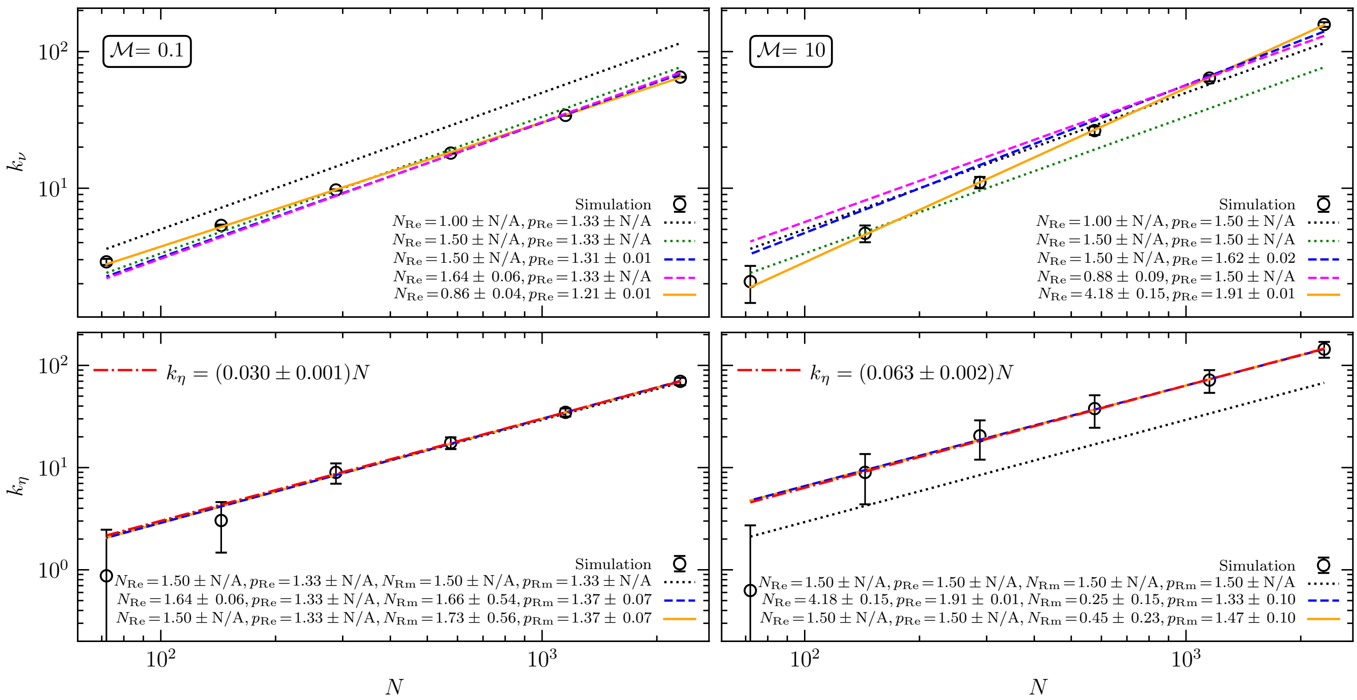

Figure 5. Viscous dissipation wave number k_ν obtained from $P_{\rm kin}$ (top panels; column 11 in Tab. 1), and the resistive dissipation wave number k_η obtained from $P_{\rm mag}$ (bottom panels; column 12 in Tab. 1), in units of $k_{\rm box}$, against linear grid resolution N, along with their 2-sigma variations displayed as error bars. The left and right panels belong to the subsonic and supersonic regimes, respectively. We find that k_ν for $\mathcal{M} = 0.1$ and k_η for both subsonic and supersonic regimes vary linearly with N, well within the error bars, and k_ν for $\mathcal{M} = 10$ varies slightly super-linearly with N. We fit Eq. (18) to k_η to determine the proportionality constant in the linear relation between k_η and N (see legend in the top left corner of the bottom panels). Eqs. (17) and (21) are fitted (taking the 2-sigma variations into account) to k_ν and k_η, respectively, to extract the corresponding parameters (shown in the legends). Various different combinations of free and fixed fit parameters (where fixed parameters are indicated with N/A on the respective parameter error quoted in the legend) are presented with different colours and line styles (see legends; discussed in the text).

Therefore, using theoretical values for $p_{\rm kin}$, with $p_{\rm kin} = -5/3$ from Kolmogorov turbulence (subsonic regime), and $p_{\rm kin} = -2$ for Burgers turbulence (supersonic regime), the theoretical predictions are $p_{\rm Re} = 4/3$ and 3/2 for $\mathcal{M} = 0.1$ and 10, respectively.

From the fits in Fig. 5, we find that in the subsonic regime, Eq. (17) with $N_{\rm Re} = 1.50$ and $p_{\rm Re} = 4/3$ is a reasonable model for k_ν as a function of N, with the slope of the data being slightly shallower. A fit with $N_{\rm Re} = 1.50$ gives $p_{\rm Re} = 1.31 \pm 0.01 \approx p_{\rm Re_{theo}}$ (blue-dashed line), and $N_{\rm Re} = 1.64 \pm 0.06$ for a fit with $p_{\rm Re} = p_{\rm Re_{theo}}$ (magenta-dashed line), quantifying the data being shallower than our predictions. Therefore, even though the best fit (yellow-solid line) provides $N_{\rm Re} = 0.86 \pm 0.04$ and $p_{\rm Re} = 1.21 \pm 0.01$, we consider the magenta-dashed line to be our preferred fit for further analysis, as it provides a reasonable model (with only 1 fit parameter), especially for $N \geq 144$ (as discussed above), and follows the theoretical prediction of $p_{\rm Re} = p_{\rm Re_{theo}} = 4/3$ reasonably well.

Considering the supersonic regime, we observe that k_ν as a function of N is steeper than either of our theoretical predictions, i.e., the black-dotted line ($N_{\rm Re} = 1.0$; $p_{\rm Re} = 3/2$) and the green-dotted line ($N_{\rm Re} = 1.5$; $p_{\rm Re} = 3/2$). Therefore, we find $p_{\rm Re} > p_{\rm Re_{theo}}$ in the supersonic regime. This is quantified by the best-fit line with $p_{\rm Re} = 1.91 \pm 0.01$ being $\sim 27\%$ larger than $p_{\rm Re_{theo}} = 3/2$, and $N_{\rm Re} = 4.18 \pm 1.91$. This result suggests that k_ν in the supersonic regime varies super-linearly with N, with Rm = 1 occurring at a larger number of cells ($N_{\rm Re} \sim 4$) for $\mathcal{M} = 10$ than for $\mathcal{M} = 0.1$ ($N_{\rm Re} \sim 1.5$).

In conclusion, while the results of the dependence of k_ν on N in the subsonic regime agree with the predicted value of $p_{\rm Re}$, $p_{\rm Re}$ is found to be $\sim 27\%$ larger than the theoretical value (3/2) for $\mathcal{M} = 10$. We discuss this further in Appendix B.

4.1.2.2 Resistive dissipation scale (k_η). As discussed above, we find that k_η varies linearly with N, irrespective of $\mathcal{M}$ (see red dot-dashed lines in the bottom panels of Fig. 5). From Eq. (21), we proceed to obtain Eqs. (C9) and (C12) between $p_{\rm Rm}$ and $p_{\rm Re}$ for $\mathcal{M} = 0.1$ and 10, respectively, which obeys the linear relation between k_η and N (see Appendix C). This implies that for $p_{\rm Re} = p_{\rm Re_{theo}}$, we must have $p_{\rm Rm} = p_{\rm Re}$ (irrespective of $\mathcal{M}$).

We note that in the bottom panels of Fig. 5, the errors in $N_{\rm Re}$ and $p_{\rm Re}$ do not imply that these parameters were allowed to vary in that particular fit, but are the errors carried over from the corresponding parameter values in the top panels. For the plots of k_η vs. N, the dotted lines represent our theoretical predictions with $N_{\rm Re} = N_{\rm Rm} = 1.50$ and $p_{\rm Re} = p_{\rm Rm} = p_{\rm Re_{theo}}$. The blue-dashed line fixes $N_{\rm Re}$ and $p_{\rm Re}$ with values from the preferred fits of k_ν vs. N, for the respective $\mathcal{M}$ number regime. The yellow solid line fixes $N_{\rm Re} = 1.5$ and $p_{\rm Re} = p_{\rm Re_{theo}}$.

Considering the linear dependence of k_η on N in the subsonic regime, we note that the coefficient of the fit is 0.030 ± 0.001. We find that our theoretical prediction with $p_{\rm Re_{theo}} = 4/3$ fits the data very well within the error bars, i.e., 2-sigma variations, and provides a slope of 0.029 for the linear relation. From the fits shown as the blue dashed line, we find $N_{\rm Re} \approx N_{\rm Rm}$ and $p_{\rm Rm} \approx p_{\rm Re} = p_{\rm Re_{theo}}$, within the error bars. From the fit shown as the yellow solid line, we find $p_{\rm Rm} \approx p_{\rm Re} = p_{\rm Re_{theo}}$ within the error bars. We note that the obtained values of $p_{\rm Rm}$ abide by Eq. (C9), and all the fits agree with

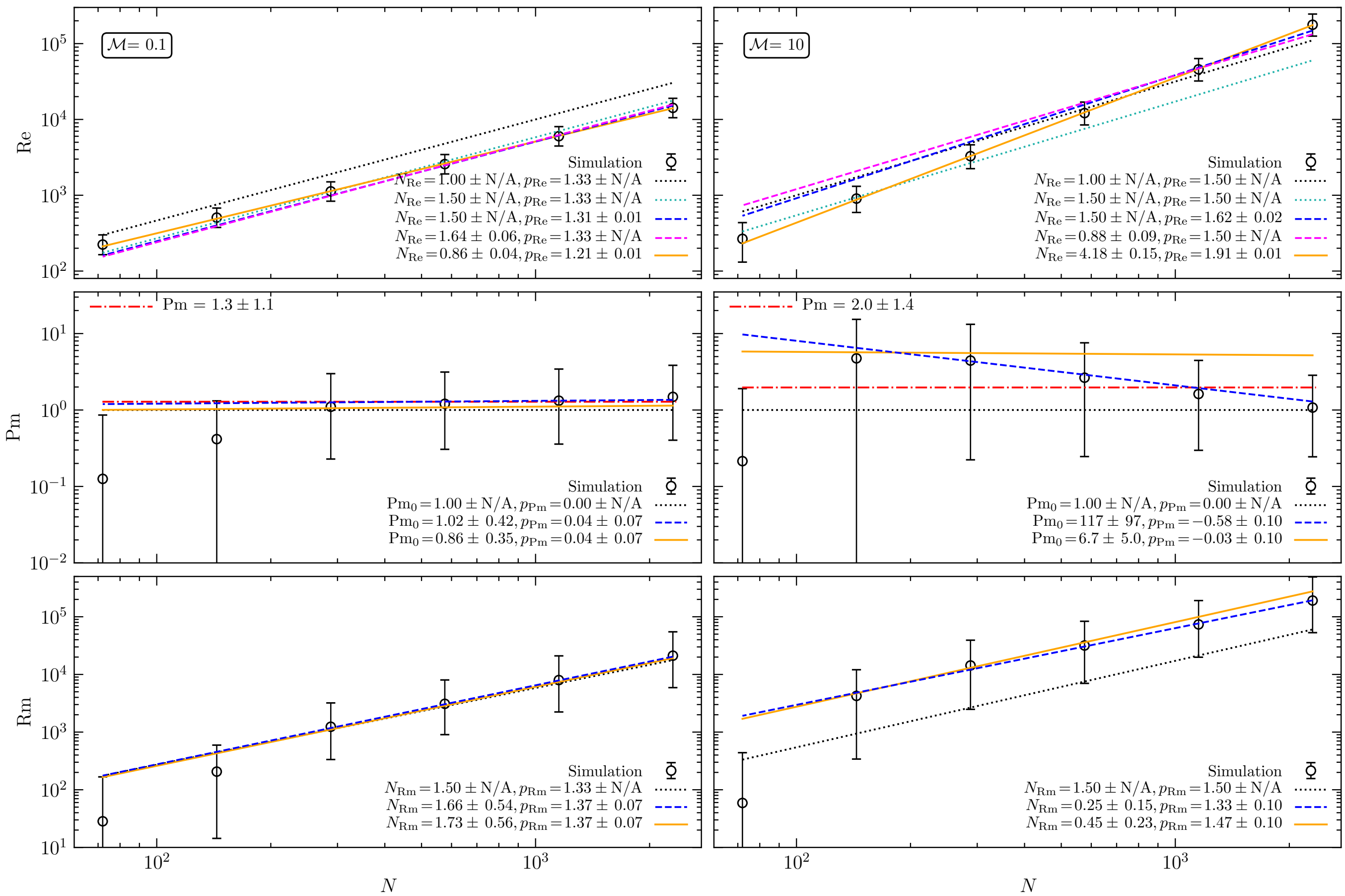

Figure 6. Hydrodynamic Reynolds number Re calculated from k_ν (top panels; column 13 of Tab. 1), magnetic Prandtl number Pm calculated from k_ν and k_η (bottom panels; column 14 of Tab. 1), and magnetic Reynolds number Rm calculated from Re and Pm (middle panels; column 15 of Tab. 1), against N. Eqs. (16), (20), and (25) are plotted with fixed parameters from Fig. 5. We find in the subsonic regime that the exponent of the power-law exponent $p_{\rm Re}$ of the Re scaling with N follows Eq. (22), abiding by the predictions of Kolmogorov turbulence, but in the supersonic case, $p_{\rm Re} = 1.91$ which is considerably larger than the predictions of Burgers turbulence (as discussed and reflected in Fig. 5). We observe that $p_{\rm Rm}$ takes on the value of $p_{\rm Re}$ as per Eq. (22), in the scaling of Rm with N, for both $\mathcal{M} = 0.1$ and 10, within the 2-sigma variations. We note that Pm is nearly constant in the subsonic regime, and scales as $\sim N^{-0.58\pm0.10}$ in the supersonic regime. We also fit a constant (i.e., Pm = constant) and obtain 1.3 ± 1.1 for $\mathcal{M} = 0.1$, and 2.0 ± 1.4 for $\mathcal{M} = 10$, shown as red dash-dotted lines.

the linear relation between k_η and N (Eq. 18), with $N_{\rm Re} \approx N_{\rm Rm}$ and $p_{\rm Rm} \approx p_{\rm Re}$ within the error bars.

For the supersonic regime, we find the coefficient of the linear dependence of k_η on N to be 0.063 ± 0.002. We find that the simplest theoretical prediction (black dotted line) falls a factor of ~ 2 below the k_η simulation data. By contrast, the model fits represented by the blue dashed line and the yellow solid line follow the data very well, and reproduce the linear relation between k_η and N. However, while the blue dashed line is a good fit, the associated $p_{\rm Re} = 1.91$ and $p_{\rm Rm} = 1.33$ do not follow Eq. (C12), which predicts $p_{\rm Rm} = 1.045$ for $p_{\rm Re} = 1.91$. This problem is absent from the model represented by the yellow solid line, for which $p_{\rm Rm} \approx p_{\rm Re} = p_{\rm Re_{theo}}$. Therefore, we prefer this model for the dependence of k_η on N, however, noting the caveat that the data for k_ν (respective top panel of Fig. 5) prefers $p_{\rm Re} \sim 1.9$. We will discuss reasons for the steeper-than-theoretical dependence of k_ν on N below. We also note in this context that k_η has a weaker dependence on Re than on Rm, i.e., $k_\eta \propto k_\nu \mathrm{Pm}^{1/2} \propto \mathrm{Re}^{1/p_{\rm Re}-1/2}\mathrm{Rm}^{1/2}$ (Eqs. 19 and 15). Therefore, k_η is not as sensitive to $p_{\rm Re}$ compared to k_ν, and thus, we obtain good linear relations for k_η with N even for the supersonic case, where the data in the top right panel of Fig. 5 suggests $p_{\rm Re} \sim 1.9$.

4.2 Dependence of Re, Rm and Pm on N

Here we determine the dependence of the hydrodynamic Reynolds number Re and the magnetic Reynolds number Rm on the grid resolution N in ideal-MHD simulations, which quantify the numerical viscous and resistive dissipation, respectively.

Re as a function of k_ν, obtained by rearranging Eq. (15), is given by

$$\mathrm{Re} = \left(\frac{k_\nu}{c_\nu k_{\rm turb}}\right)^{p_{\rm Re_{theo}}}. \tag{23}$$

Similarly, the magnetic Prandtl number Pm as a function of k_η and k_ν, obtained by rearranging Eq. (19), is given by

$$\mathrm{Pm} = \left(\frac{k_\eta}{c_\eta k_\nu}\right)^2. \tag{24}$$

From Eqs. (23), (24), and (3), we compute the values of Re, Pm and the corresponding Rm, along with their errors, using Monte–Carlo error propagation. The results are listed in columns 13, 14 and 15 of Tab. 1, respectively (see §4.1).

The resulting values of Re, Rm, and Pm are shown in Fig. 6, following the same basic figure organisation as in Fig. 5. We emphasise that no further fitting has been performed in Fig. 6. However, this presentation of the results allows us to directly show the relations of Re, Rm, and Pm as a function of N (as opposed to k_ν and k_η as a function of N in Fig. 5).

4.2.0.1 Hydrodynamic Reynolds number (Re). We start by considering Re as a function of N. This is shown in the top panels of Fig. 6, with the left and right panels belonging to $\mathcal{M} = 0.1$ and 10, respectively. The fits shown in the plot of Re as a function of N follow Eq. (16) with fixed parameters taken from k_ν vs. N. Therefore, the errors of the parameters shown in the legend do not imply that the parameters are left to vary unlike in §4.1, but they simply display the errors obtained from the fits in Fig. 5. With this in mind, we observe that the parameters obtained for the dependence of k_ν on N fit that of Re, within the error bars. Therefore, in the subsonic case, the exponent of Eq. (16) (p_{Re}) follows the prediction of Eq. (22), whereas in the supersonic case, p_{Re} is 27% higher than the expectation from Burgers turbulence.

4.2.0.2 Magnetic Prandtl number (Pm). To study any potential (albeit weak) variation of Pm with N, we define

$$\mathrm{Pm} = \mathrm{Pm}_0\, N^{p_{\mathrm{Pm}}}, \tag{25}$$

where $\mathrm{Pm}_0 = \mathrm{Pm}$ when $N = 1$. From Eqs. (16) and (20), we obtain

$$p_{\mathrm{Pm}} = p_{\mathrm{Rm}} - p_{\mathrm{Re}}, \tag{26}$$

$$\mathrm{Pm}_0 = N_{\mathrm{Re}}^{p_{\mathrm{Re}}} / N_{\mathrm{Rm}}^{p_{\mathrm{Rm}}}. \tag{27}$$

With no further fitting done, we calculate p_{Pm} and Pm_0, and their corresponding errors. We consider N_{Re} and p_{Re} from the magenta and yellow lines of the top panels, and N_{Rm} and p_{Rm} from the bottom panels of Fig. 6 for this process, to produce the blue and yellow lines of Pm, respectively, shown in the middle panels of Fig. 6. We note that from Eq. (26), if $p_{\mathrm{Re}} = p_{\mathrm{Rm}}$, it automatically follows that Pm is independent of N. This is depicted by the black dotted lines for both $\mathcal{M} = 0.1$ and 10, where we also picked $N_{\mathrm{Re}} = N_{\mathrm{Rm}} = 1.50$, resulting in $\mathrm{Pm} = 1$. We note that Pm is nearly constant ~ 1 for the subsonic regime and scales with $N^{-0.58\pm0.10}$ in the supersonic regime, considering the blue-dashed line.

Having explored the weak dependence of Pm on N, we note that overall, Pm is largely consistent with a constant value in the subsonic and supersonic regimes, within the 2-sigma variations. Therefore, we also fit a constant (i.e., Pm = constant) and obtain 1.3 ± 1.1 for $\mathcal{M} = 0.1$, and 2.0 ± 1.4 for $\mathcal{M} = 10$. These are shown as red dash-dotted lines in Fig. 6.

4.2.0.3 Magnetic Reynolds number (Rm). The bottom panels of Fig. 6 show Rm based on Eq. (20) with parameters N_{Rm} and p_{Rm} taken from k_η vs. N. In the subsonic regime, we note that all models fit the data of Rm within the error bars. Therefore, we observe that the scaling of Rm with N is with an exponent $p_{\mathrm{Rm}} = p_{\mathrm{Re_{theo}}}$. For the supersonic regime, we note that the blue dashed line ($p_{\mathrm{Rm}} = 1.33$) best fits the obtained data points, as the black dotted and yellow solid lines are slightly steeper.

4.2.0.4 Summary. We determined the dependence of the Reynolds numbers (Re and Rm), and the magnetic Prandtl number (Pm), on the linear grid resolution (N), for simulations with purely numerical viscosity and resistivity. We note that different MHD solvers may use different approximations and methods for computing solutions to the MHD equations. Therefore, the extracted micro-scales (N_{Re} and N_{Rm}) may differ somewhat (we expect variations by factor $\lesssim 2$ in state-of-the-art schemes) with different grid-based solvers. However, the dependence on N will be very similar for different solvers and codes, as the N-dependent numerical dissipation is a universal property of any grid-based MHD scheme.

5 COMPARISON TO SIMULATION DATA IN THE LITERATURE

In order to better understand the significance of the present findings and how they relate to other works, we start by comparing our results to recent simulations in Grete et al. (2023). Grete et al. (2023) find relations between the numerical viscosity ν and resistivity η, and the grid spacing Δ_x, i.e., $\nu \propto \Delta_x^{1.22}$ and $\eta \propto \Delta_x^{1.34}$, obtained from ILES simulations in the subsonic regime, similar to our $\mathcal{M} = 0.1$ simulations (see their figure 5). With u_{turb} and ℓ_{turb} fixed in an MHD simulation, we can rewrite these relations, using Eqs. (1) and (2), as:

$$\nu \propto \Delta_x^{p_{\mathrm{Re}}} \propto N^{-p_{\mathrm{Re}}} \propto \mathrm{Re}^{-1}, \tag{28}$$

$$\eta \propto \Delta_x^{p_{\mathrm{Rm}}} \propto N^{-p_{\mathrm{Rm}}} \propto \mathrm{Rm}^{-1}, \tag{29}$$

as $N = L_{\mathrm{box}}/\Delta_x$, where L_{box} is the side length of the box (computational domain).

Thus, Grete et al. (2023) found $p_{\mathrm{Re}} = 1.22$ and $p_{\mathrm{Rm}} = 1.34$, which is in agreement with $p_{\mathrm{Re}} \in [1.20, 1.33]$ and $p_{\mathrm{Rm}} \in [1.30, 1.44]$ obtained from all of the fits tested on our simulations (see Fig. 6) in the subsonic regime. In order to find the parameters N_{Re} and N_{Rm} for Grete et al. (2023)'s data, we fit Re and Rm to Grete et al. (2023)'s simulations, as a function of N, using Eqs. (16) and (20), respectively. We plot the resulting model as the indigo-dashed line in Fig. 7, alongside Grete et al. (2023)'s data, and our data and best fit model (c.f., Fig. 6; fit parameters are displayed in the legends in the bottom-right corner of Fig. 7). We see that the $N_{\mathrm{Re}} \in [0.80, 1.70]$ and $N_{\mathrm{Rm}} \in [1.50, 2.50]$ obtained from our simulations are larger than $N_{\mathrm{Re}} = 0.63 \pm 0.01$ and $N_{\mathrm{Rm}} = 0.92 \pm 0.02$, obtained from the fits to Grete et al. (2023)'s data, by about a factor of 2. This difference in N_{Re} and N_{Rm} between our simulations and Grete et al.'s simulations is a result of the MHD solver and code used in Grete et al. (2023) compared to the numerical methods used here. While Grete et al. (2023) use a predictor-corrector, van Leer-type integrator, with the HLLD Riemann solver, and constrained transport, we use a modified version of the `FLASH` code utilising a 5-wave, approximate Riemann solver with divergence cleaning (see §2.1). This suggests that the numerical MHD scheme used in Grete et al. (2023) is somewhat less dissipative than the numerical scheme used here. However, we emphasise that this factor of ~ 2 difference is relatively small, compared to the dependence of Re and Rm on the grid resolution N, for which our simulations agree with those by Grete et al. (2023).

In order to understand the importance of reliable estimates of the numerical Reynolds numbers, we show the Re, Pm and Rm values that were set as target values (by explicitly setting ν and η in Eqs. 5 and 6) in DNS simulations of various studies in the literature. These data are also shown in Fig. 7, with abbreviations of the literature sources in the top-left legend of the top panels for $\mathcal{M} = 0.1$ and 10. These literature sources, in the order displayed (increasing order of publication year) for $\mathcal{M} = 0.1$ are SCT+(04): (Schekochihin et al. 2004b), HB(04): (Haugen & Brandenburg 2004), HBD(04): (Haugen et al. 2004a), HBM(04): (Haugen et al. 2004b), MB(06): (Mee & Brandenburg 2006), SIC+(07): (Schekochihin et al. 2007), FCS+(11): (Federrath et al. 2011a), BR(19): (Brandenburg & Rempel 2019), AFT+(21): (Achikanath Chirakkara et al. 2021), SF(21): (Seta & Federrath 2021), KBS+(22): (Kriel et al. 2022), GKW+(22): (Galishnikova et al. 2022), and BFK+(23): (Beattie et al. 2023). Similarly, for $\mathcal{M} = 10$, the works included are FCS+(11):

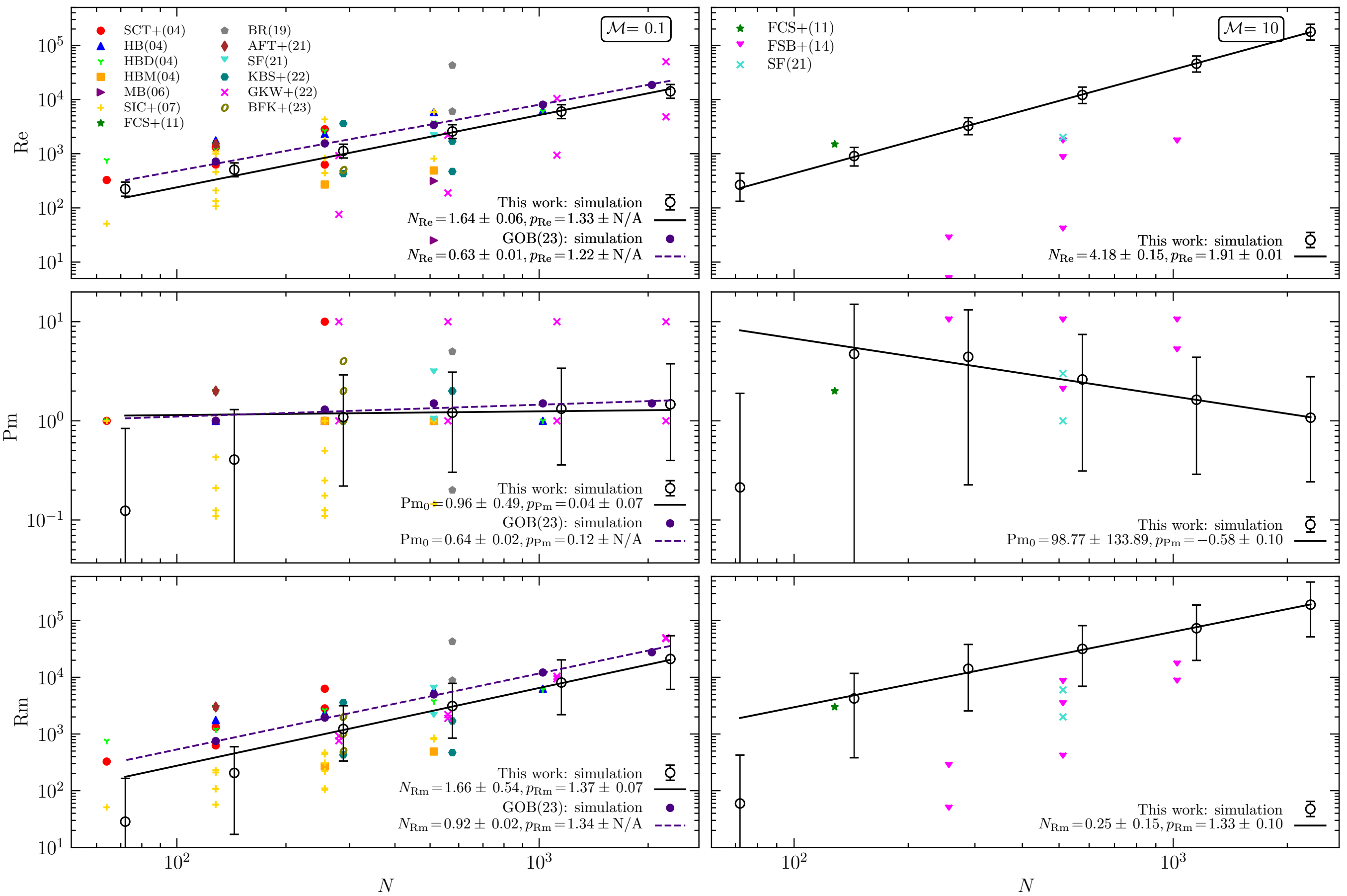

Figure 7. Hydrodynamic Reynolds number (Re, top panels), magnetic Prandtl number (Pm, middle panels), and magnetic Reynolds number (Rm, bottom panels) set for a particular grid resolution N in published DNS simulation studies (see legends in the top-left corner in the top panels), plotted alongside the numerical Re, Pm, and Rm models determined in the present work (corresponding parameters shown in legends the bottom-right corner in each panel), for the subsonic regime (left panels) and the supersonic regime (right panels). Data points from the literature in the order displayed in the legend are – for the subsonic regime: SCT+(04): (Schekochihin et al. 2004b), HB(04): (Haugen & Brandenburg 2004), HBD(04): (Haugen et al. 2004a), HBM(04): (Haugen et al. 2004b), MB(06): (Mee & Brandenburg 2006), SIC+(07): (Schekochihin et al. 2007), FCS+(11): (Federrath et al. 2011a), BR(19): (Brandenburg & Rempel 2019), AFT+(21): (Achikanath Chirakkara et al. 2021), SF(11): (Seta & Federrath 2021), KBS+(22): (Kriel et al. 2022), GKW+(22): (Galishnikova et al. 2022), and BFK+(23): (Beattie et al. 2023); and for the supersonic regime: FCS+(11): (Federrath et al. 2011a), FSB+(14): (Federrath et al. 2014), and SF(11): (Seta & Federrath 2021). For the subsonic regime we also show Re, Pm, and Rm obtained from ILES simulations in Grete et al. (2023) (GOB(23)) as indigo-filled circles, and their respective fit relations are shown as indigo dashed lines, for comparison with the respective ILES results obtained in the present study (black open circles and black solid lines) – see legends in the bottom-right corners of the left-hand panels.

(Federrath et al. 2011a), FSB+(14): (Federrath et al. 2014), and SF(21): (Seta & Federrath 2021).

As a general rule, in order to keep the numerical dissipation effects minimal, the explicit dissipation terms have to be chosen such that they exceed the numerical viscosity and resistivity, e.g., the target explicit Reynolds numbers for a particular N must be set to a value smaller than the corresponding numerical value of Re and Rm determined by ILES in this and Grete et al.'s work. This ensures that the target Re and Rm is actually resolved for a given N. On the contrary, if N is too small for a set target Re and Rm, then the actual Re and Rm will be limited by numerical dissipation as quantified in the ILES relations derived in Figs. 6 and 7. We see that most of the target Re and Rm set in DNS simulations in the literature are close to their maximum achievable values, i.e., the numerical Re and Rm for a particular N. However, some published simulations set target Re and Rm values below the numerical ones, while other simulations have targets exceeding the numerical values of Re and Rm for a given N. The former have dissipation and Re and Rm well resolved, while the latter may effectively have lower Re and Rm than their target values set in the simulations.

Therefore, the present study provides relations between the numerical Re and Rm as a function of N, which may provide users with an estimate of the grid resolution required to achieve target explicit Reynolds numbers. While we have seen that the exact value of N_{Re} and N_{Rm} depends somewhat on the details of the numerical solvers and MHD schemes used in a particular code (c.f., the ILES simulations in this work compared to the work by Grete et al. 2023: solid vs. dashed lines in Fig. 7), the numerical dissipation primarily depends on the grid resolution N, and we do not expect other grid-based codes to show substantially different scaling exponents (p_{Re} and p_{Rm}) or normalisation constants (N_{Re} and N_{Rm}).

6 SUMMARY AND CONCLUSIONS

We determined the effective hydrodynamic Reynolds number (Re), the magnetic Prandtl number (Pm), and the magnetic Reynolds number (Rm) as a function of linear grid resolution (N), from MHD simulations with purely numerical viscosity and resistivity, i.e., in Implicit Large Eddy Simulations (ILES). To do so, we studied the kinetic and magnetic power spectra in the kinematic phase of the turbulent dynamo. Throughout the study, we distinguish the subsonic ($\mathcal{M} = 0.1$) and the supersonic ($\mathcal{M} = 10$) regime of turbulence. We summarise our results as follows:

- Through the time evolution of the magnetic-to-kinetic energy ratio ($E_{\mathrm{mag}}/E_{\mathrm{kin}}$) in the kinematic phase of the dynamo (see Fig. 1), we show that the rate of growth of the magnetic field increases with the linear grid resolution N (c.f., column 2 of Tab. 1). The qualitative differences in the magnetic field morphology between the subsonic and supersonic regimes in Figs. 2 and 3 demonstrate that smaller-scale magnetic field structures are increasingly resolved with improved grid resolution. This implies that the amplification of the magnetic field increases with increasing N.
- In order to quantify the above qualitative findings, we perform spectral (Fourier) analysis on the time-averaged kinetic (P_{kin}) and magnetic (P_{mag}) power spectra (see Fig. 4) obtained from our simulations. To determine the viscous (k_ν) and resistive (k_η) dissipation wave numbers, we fit model spectra to the simulations (see Eqs. 10 and 11). The extracted k_ν and k_η from P_{kin} and P_{mag} (see columns 11 and 12 of Tab. 1) quantify our previous findings, i.e., the dissipation scales and the associated Reynolds numbers depend on the grid resolution N.
- In order to quantify the N-dependence of the dissipation wave numbers and the associated Reynolds numbers, we fit k_ν and k_η as functions of N (see Fig. 5) with the formulations proposed from the theory of turbulence (Kolmogorov and Burgers turbulence for the subsonic and supersonic regimes, respectively; see Eqs. (17) and (21), and Appendix D), and translate that information to Fig. 6 to show Re, Pm, and Rm as functions of N.
- While the results of k_ν and Re as functions of N are in agreement with the predictions of Kolmogorov turbulence ($p_{\mathrm{Re}} = 4/3$) in the subsonic regime, the measured $p_{\mathrm{Re}} = 1.91 \pm 0.01$ for the supersonic regime exceeds the expectation of Burgers turbulence ($p_{\mathrm{Re}} = 3/2$) by $\sim 27\%$. Overall, we find that $\mathrm{Re} = (N/N_{\mathrm{Re}})^{p_{\mathrm{Re}}}$, with $p_{\mathrm{Re}} \in [1.2, 1.4]$ and $N_{\mathrm{Re}} \in [0.8, 1.7]$ in the subsonic regime, and with $p_{\mathrm{Re}} \in [1.5, 2.0]$ and $N_{\mathrm{Re}} \in [0.8, 4.4]$ in the supersonic regime. The ranges here (and in the following) are obtained by considering the minimum and maximum of the 1-sigma range over all the plausible models.
- We further find that k_η is a linear function of N with the coefficients being 0.030 ± 0.001 in the subsonic regime and 0.063 ± 0.002 in supersonic regime. Related to this, we find that $\mathrm{Rm} = (N/N_{\mathrm{Rm}})^{p_{\mathrm{Rm}}}$, with $p_{\mathrm{Rm}} \in [1.3, 1.5]$ and $N_{\mathrm{Rm}} \in [1.1, 2.3]$ in the subsonic regime, and with $p_{\mathrm{Rm}} \in [1.2, 1.6]$ and $N_{\mathrm{Rm}} \in [0.1, 0.7]$ in the supersonic regime.
- Formally, we find a weak dependence of Pm on N. However, our data is also consistent with constant values of 1.3 ± 1.1 for $\mathcal{M} = 0.1$, and 2.0 ± 1.4 for $\mathcal{M} = 10$.
- In order to put these results into a broader context, we compare them to figure 5 in Grete et al. (2023), restricted to the subsonic regime (Grete et al. 2023 only investigated subsonic turbulence). We find that while N_{Re} and N_{Rm} obtained from our simulations are larger than the ones obtained from our fits to Grete et al.'s data by a factor of ~ 2, which is due to the differences in the MHD solver and code used in both works, the dependence of Re and Rm on N, i.e., p_{Re} and p_{Rm}, agrees well in both data sets.
- We show the target explicit Re, Pm, and Rm from simulations with explicit viscosity and resistivity (i.e., in Direct Numerical Simulations, DNS) from various works in the literature together with the ILES data from this work and from Grete et al. (2023), and together with the respective model functions of N in Fig. 7. This comparison and our relations can be used to estimate the effective Re, Rm and Pm for a given N, and to check whether a particular target Reynolds number can be achieved at a given N.

We conclude that for numerical simulations of turbulence to converge to the intended physical conditions, the explicit (target, DNS) Reynolds numbers (Re, and for magnetised flows, also Rm) must be set such that they are below the corresponding numerical (ILES) Reynolds numbers (obtained from the present work and Grete et al. 2023) in Fig. 6 for a chosen numerical grid resolution N.

ACKNOWLEDGEMENTS

L. M. is supported by a Kishore Vaigyanik Protsahan Yojana (KVPY) scholarship. C. F. acknowledges funding provided by the Australian Research Council (Future Fellowship FT180100495 and Discovery Project DP230102280), and the Australia-Germany Joint Research Cooperation Scheme (UA-DAAD). We further acknowledge high-performance computing resources provided by the Leibniz Rechenzentrum and the Gauss Centre for Supercomputing (grants pr32lo, pr48pi and GCS Large-scale project 10391), the Australian National Computational Infrastructure (grant ek9) and the Pawsey Supercomputing Centre (project pawsey0810) in the framework of the National Computational Merit Allocation Scheme and the ANU Merit Allocation Scheme. The simulation software, `FLASH`, was in part developed by the Flash Centre for Computational Science at the Department of Physics and Astronomy of the University of Rochester.

DATA AVAILABILITY

The simulation data underlying this paper will be shared on reasonable request to the corresponding author.

REFERENCES

Achikanath Chirakkara R., Federrath C., Trivedi P., Banerjee R., 2021, Phys. Rev. Lett., 126, 091103
Balsara D. S., Kim J., Mac Low M., Mathews G. J., 2004, ApJ, 617, 339
Beattie J. R., Federrath C., Kriel N., Mocz P., Seta A., 2023, MNRAS, 524, 3201
Beck R., Wielebinski R., 2013, in Oswalt T. D., Gilmore G., eds, , Vol. 5, Planets, Stars and Stellar Systems. Volume 5: Galactic Structure and Stellar Populations. p. 641, doi:10.1007/978-94-007-5612-0_13
Bodenheimer P., ed. 2007, Numerical Methods in Astrophysics: An Introduction
Bouchaud J. P., Mézard M., Parisi G., 1995, Phys. Rev. E, 52, 3656
Bouchut F., Klingenberg C., Waagan K., 2007, Numerische Mathematik, 108, 7
Bouchut F., Klingenberg C., Waagan K., 2010, Numerische Mathematik, 115, 647
Brandenburg A., Rempel M., 2019, ApJ, 879, 57
Brandenburg A., Subramanian K., 2005, Phys. Rep., 417, 1
Burgers J. M., 1948, Advances in Applied Mechanics, 1, 171
Dumbser M., Balsara D. S., Tavelli M., Fambri F., 2019, International Journal for Numerical Methods in Fluids, 89, 16
Elmegreen B. G., Scalo J., 2004, ARA&A, 42, 211
Ertesvåg I. S., Magnussen B. F., 2000, Combustion science and technology, 159, 213
Eswaran V., Pope S. B., 1988, Computers and Fluids, 16, 257

Falkovich G., 1994, Physics of Fluids, 6, 1411
Federrath C., 2013, MNRAS, 436, 1245
Federrath C., 2015, MNRAS, 450, 4035
Federrath C., 2016, Journal of Plasma Physics, 82, 535820601
Federrath C., 2018, Physics Today, 71, 38
Federrath C., Roman-Duval J., Klessen R. S., Schmidt W., Mac Low M. M., 2010, A&A, 512, A81
Federrath C., Chabrier G., Schober J., Banerjee R., Klessen R. S., Schleicher D. R. G., 2011a, Phys. Rev. Lett., 107, 114504
Federrath C., Sur S., Schleicher D. R. G., Banerjee R., Klessen R. S., 2011b, ApJ, 731, 62
Federrath C., Schober J., Bovino S., Schleicher D. R. G., 2014, ApJ, 797, L19
Federrath C., Klessen R. S., Iapichino L., Beattie J. R., 2021, Nature Astronomy, 5, 365
Federrath C., Roman-Duval J., Klessen R. S., Schmidt W., Mac Low M. M., 2022, TG: Turbulence Generator, Astrophysics Source Code Library, record ascl:2204.001 (ascl:2204.001)
Ferrière K. M., 2001, Reviews of Modern Physics, 73, 1031
Frisch U., 1995, Turbulence. The legacy of A.N. Kolmogorov
Galishnikova A. K., Kunz M. W., Schekochihin A. A., 2022, Physical Review X, 12, 041027
Gargett A. E., 1989, Annual Review of Fluid Mechanics, 21, 419
Giusti A., Mastorakos E., 2019, Flow, Turbulence and Combustion, 103, 847
Goto S., 2008, Journal of Fluid Mechanics, 605, 355
Grete P., O'Shea B. W., Beckwith K., 2023, ApJ, 942, L34
Haugen N. E. L., Brandenburg A., 2004, Phys. Rev. E, 70, 036408
Haugen N. E., Brandenburg A., Dobler W., 2004a, Phys. Rev. E, 70, 016308
Haugen N. E. L., Brandenburg A., Mee A. J., 2004b, MNRAS, 353, 947
Hennebelle P., Falgarone E., 2012, A&ARv, 20, 55
Hew J. K. J., Federrath C., 2023, MNRAS, 520, 6268
Igali D., Mukhmetov O., Zhao M., Fok S., Teh L., 2019, International Journal of Automotive Technology, 20, 6
Jones C. A., 2011, Annual Review of Fluid Mechanics, 43, 583
Kazantsev A. P., Ruzmaikin A. A., Sokolov D. D., 1985, Zhurnal Eksperimentalnoi i Teoreticheskoi Fiziki, 88, 487
Kida S., Murakami Y., 1987, Physics of Fluids, 30, 2030
Kitsionas S., et al., 2009, A&A, 508, 541
Kochukhov O., 2021, A&ARv, 29, 1
Kolmogorov A. N., 1941, Dokl. Akad. Nauk SSSR, 32, 16
Kolmogorov A. N., 1962, Journal of Fluid Mechanics, 13, 82
Kolmogorov A. N., 1991a, Proceedings of the Royal Society of London Series A, 434, 9
Kolmogorov A. N., 1991b, Proceedings of the Royal Society of London Series A, 434, 15
Kriel N., Beattie J. R., Seta A., Federrath C., 2022, MNRAS, 513, 2457
Kriel N., Beattie J. R., Federrath C., Krumholz M. R., Hew J. K. J., 2023, MNRAS, p. arXiv:2310.17036
Kritsuk A. G., Norman M. L., Padoan P., Wagner R., 2007, ApJ, 665, 416
Kritsuk A. G., et al., 2011, ApJ, 737, 13
Kulsrud R. M., Zweibel E. G., 2008, Reports on Progress in Physics, 71, 046901
Laney C. B., 1998, Computational gasdynamics. Cambridge university press
Lazarian A., Eyink G. L., Jafari A., Kowal G., Li H., Xu S., Vishniac E. T., 2020, Physics of Plasmas, 27, 012305
Leggett J., Zhao Y., Sandberg R. D., 2022, Journal of Turbomachinery, 145
Mac Low M.-M., Klessen R. S., 2004, Reviews of Modern Physics, 76, 125
McKee C. F., Ostriker E. C., 2007, ARA&A, 45, 565
Mee A. J., Brandenburg A., 2006, MNRAS, 370, 415
Obergaulinger M., Cerdá-Durán P., Müller E., Aloy M. A., 2009, A&A, 498, 241
Padoan P., Federrath C., Chabrier G., Evans II N. J., Johnstone D., Jørgensen J. K., McKee C. F., Nordlund Å., 2014, in Beuther H., Klessen R. S., Dullemond C. P., Henning T., eds, Protostars and Planets VI. University of Arizona Press, pp 77–100 (arXiv:1312.5365), doi:10.2458/azu_uapress_9780816531240-ch004
Park H., Linton D., Thornber B., 2022, International Journal of Heat and Fluid Flow, 93, 108916
Penna R. F., McKinney J. C., Narayan R., Tchekhovskoy A., Shafee R., McClintock J. E., 2010, MNRAS, 408, 752
Price D. J., Federrath C., 2010, MNRAS, 406, 1659
Rembiasz T., Obergaulinger M., Cerdá-Durán P., Aloy M.-Á., Müller E., 2017, ApJS, 230, 18
Rincon F., 2019, Journal of Plasma Physics, 85, 205850401
Ruzmaikin A. A., Sokolov D. D., Shukurov A. M., 1988, Magnetic Fields of Galaxies. Vol. 133, doi:10.1007/978-94-009-2835-0,
Sanada T., 1992, Physics of Fluids A, 4, 1086
Schekochihin A. A., Cowley S. C., Maron J. L., McWilliams J. C., 2004a, Phys. Rev. Lett., 92, 054502
Schekochihin A. A., Cowley S. C., Taylor S. F., Maron J. L., McWilliams J. C., 2004b, ApJ, 612, 276
Schekochihin A. A., Haugen N. E. L., Brandenburg A., Cowley S. C., Maron J. L., McWilliams J. C., 2005, ApJ, 625, L115
Schekochihin A. A., Iskakov A. B., Cowley S. C., McWilliams J. C., Proctor M. R. E., Yousef T. A., 2007, New Journal of Physics, 9, 300
Schmidt W., Federrath C., 2011, A&A, 528, A106
Schmidt W., Hillebrandt W., Niemeyer J. C., 2004, arXiv e-prints, pp astro–ph/0407616
Schmidt W., Hillebrandt W., Niemeyer J. C., 2006, Computers and Fluids, 35, 353
Schober J., Schleicher D., Federrath C., Klessen R., Banerjee R., 2012, Phys. Rev. E, 85, 026303
Schumacher J., Scheel J. D., Krasnov D., Donzis D. A., Yakhot V., Sreenivasan K. R., 2014, Proceedings of the National Academy of Science, 111, 10961
Seta A., Federrath C., 2020, MNRAS, 499, 2076
Seta A., Federrath C., 2021, Physical Review Fluids, 6, 103701
Seta A., Federrath C., 2022, MNRAS, 514, 957
Seta A., Rodrigues L. F. S., Federrath C., Hales C. A., 2021, ApJ, 907, 2
Sharda P., Federrath C., Krumholz M. R., Schleicher D. R. G., 2021, MNRAS, 503, 2014
She Z.-S., Leveque E., 1994, Phys. Rev. Lett., 72, 336
Smith L., Reynolds W., 1991, Physics of Fluids A: Fluid Dynamics, 3, 992
Sohail T., Vreugdenhil C. A., Gayen B., Hogg A. M., 2019, Journal of Geophysical Research (Oceans), 124, 4208
Stevenson D. J., 2003, Earth and Planetary Science Letters, 208, 1
Subramanian K., 2010, Astronomische Nachrichten, 331, 110
Sur S., Schleicher D. R. G., Banerjee R., Federrath C., Klessen R. S., 2010, ApJ, 721, L134
Thornber B., Mosedale A., Drikakis D., 2007, Journal of Computational Physics, 226, 1902
Verma M. K., Donzis D., 2007, Journal of Physics A Mathematical General, 40, 4401
Waagan K., Federrath C., Klingenberg C., 2011, Journal of Computational Physics, 230, 3331
Widrow L. M., 2002, Reviews of Modern Physics, 74, 775
Zamaninasab M., Clausen-Brown E., Savolainen T., Tchekhovskoy A., 2014, Nature, 510, 126

APPENDIX A: COMPENSATED KINETIC SPECTRA

Fig. A1 shows the time-averaged kinetic power spectra, compensated by k^{-2}, to visualise the quality of the fit using Eq. (10) to P_{kin}. We see that Eq. (10) is an excellent model for P_{kin}, despite fixing the values of p_{kin} and p_{ν} (see Tab. 1).

APPENDIX B: DECOMPOSED KINETIC SPECTRA IN THE SUPERSONIC REGIME

In the main part of the study, we found that k_{ν} in the supersonic regime has a stronger scaling on N than predicted by Burgers turbulence, i.e., we found $p_{\mathrm{Re}} = 1.9$ instead of $p_{\mathrm{Re}} = 3/2$. To elucidate this finding, we perform a Helmholtz decomposition and study the scaling of k_{ν} obtained from the longitudinal and transverse components

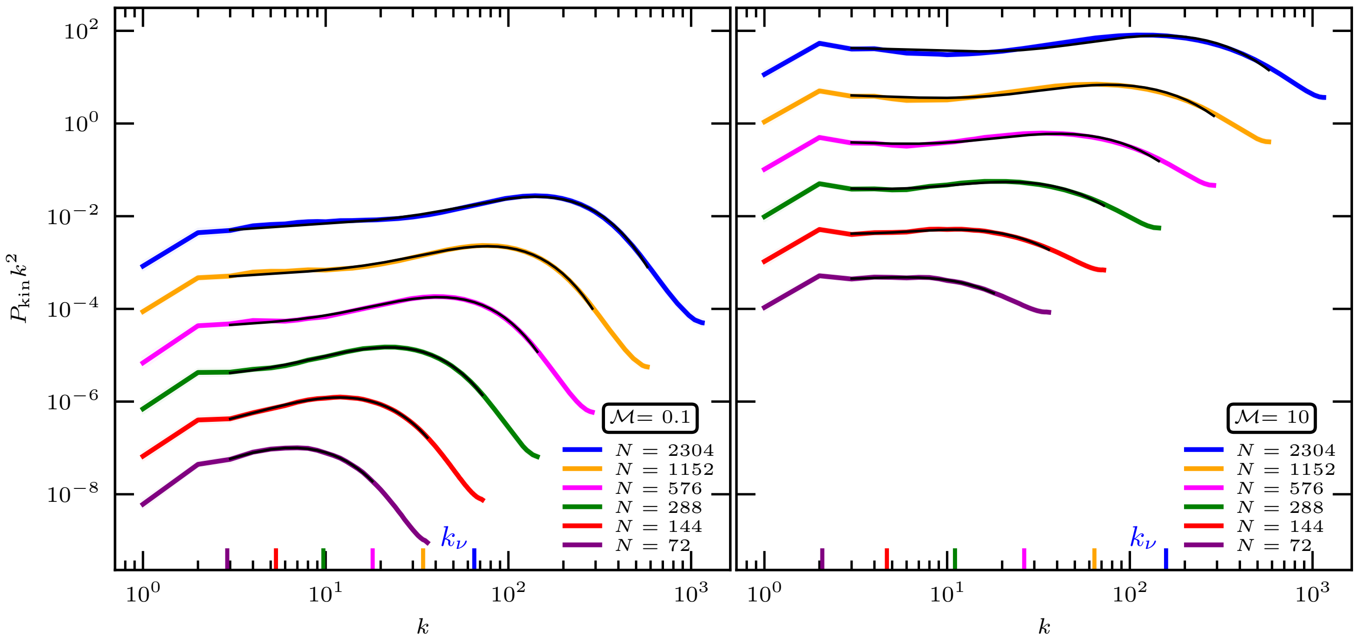

Figure A1. Same as the top panels of Fig. 4, but here the kinetic power spectra (P_{kin}) are compensated by k^{-2} to demonstrate the quality of the fit, including power-law section, Bottleneck, and dissipation range.

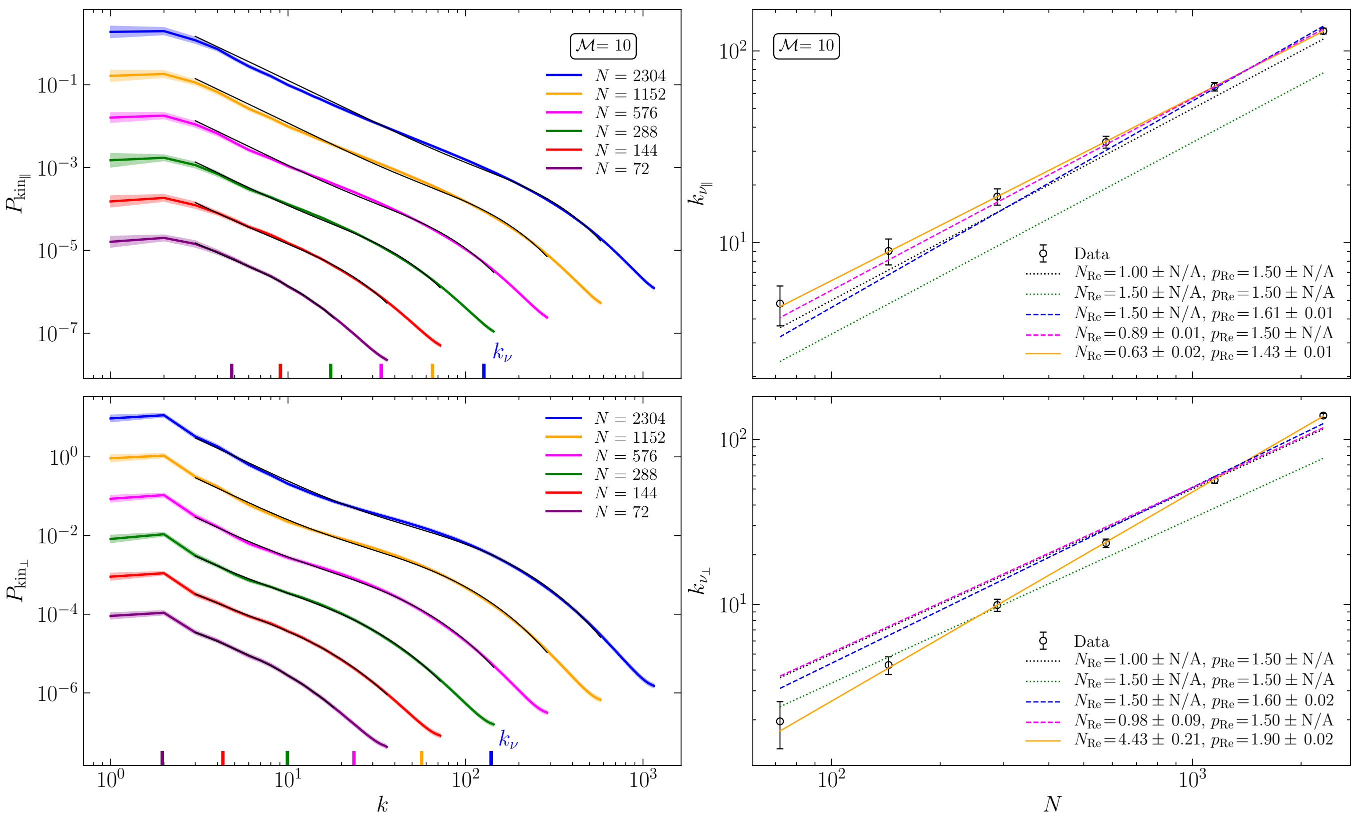

Figure B1. Same as the top right panels of Fig. 4 and Fig. 5, but here for the longitudinal (top panels; $P_{\mathrm{kin}_\parallel}$) and transverse (bottom panels; $P_{\mathrm{kin}_\perp}$) components of the kinetic spectra (left panels) in the supersonic regime, along with their respective derived viscous dissipation wave numbers (right panels; see column 7 of Tab. B1 for $k_{\nu_\parallel}$ and $k_{\nu_\perp}$). The methodology of the fitting is the same as discussed in §2.2 and §4.1.

Table B1. Kinetic parameters as in Tab. 1, but here for the decomposition of the kinetic power spectrum into its longitudinal ($P_{\mathrm{kin}_{\parallel}}$) and transverse ($P_{\mathrm{kin}_{\perp}}$) components.

$\mathcal{M} = 10$							
N (1)	p_{kin} (2)	p_{bn} (3)	p_{ν} (4)	k_{bn} (5)	$\tilde{k}_{\nu}$ (6)	k_{ν} (7)	Re (8)
From $P_{\mathrm{kin}_{\parallel}}$						**Derived**	
2304	-2.0	0.0 ± 0.0	1.0	93.4 ± 1.2	127.0 ± 2.2	127.0 ± 2.2	$1.3^{+0.3}_{-0.2} \times 10^{5}$
1152	-2.0	0.0 ± 0.2	1.0	48.2 ± 0.9	65.1 ± 1.6	65.1 ± 1.6	$4.7^{+1.0}_{-0.9} \times 10^{4}$
576	-2.0	0.0 ± 0.2	1.0	25.1 ± 0.6	33.5 ± 1.2	33.5 ± 1.2	$1.7^{+0.4}_{-0.4} \times 10^{4}$
288	-2.0	0.0 ± 0.1	1.0	13.6 ± 0.4	17.4 ± 0.8	17.4 ± 0.8	$6.5^{+2.0}_{-1.0} \times 10^{3}$
144	-2.0	0.0 ± 0.3	1.0	7.51 ± 0.41	9.05 ± 0.70	9.05 ± 0.70	$2.4^{+0.7}_{-0.6} \times 10^{3}$
72	-2.0	0.0 ± 0.2	1.0	4.24 ± 0.45	4.81 ± 0.57	4.81 ± 0.57	$9.4^{+3.0}_{-3.0} \times 10^{2}$
From $P_{\mathrm{kin}_{\perp}}$						**Derived**	
2304	-2.0	0.0 ± 0.0	0.7	24.8 ± 0.4	31.7 ± 0.3	139.0 ± 2.1	$1.5^{+0.3}_{-0.3} \times 10^{5}$
1152	-2.0	0.0 ± 0.0	0.7	14.8 ± 0.3	16.9 ± 0.2	56.6 ± 1.1	$3.8^{+0.8}_{-0.7} \times 10^{4}$
576	-2.0	0.0 ± 0.1	0.7	9.19 ± 0.27	9.12 ± 0.18	23.5 ± 0.7	$1.0^{+0.2}_{-0.2} \times 10^{4}$
288	-2.0	0.0 ± 0.0	0.7	5.74 ± 0.24	4.98 ± 0.15	9.91 ± 0.42	$2.8^{+0.7}_{-0.6} \times 10^{3}$
144	-2.0	0.0 ± 0.1	0.7	3.74 ± 0.22	2.77 ± 0.12	4.29 ± 0.26	$8.0^{+2.0}_{-2.0} \times 10^{2}$
72	-2.0	0.0 ± 0.2	0.7	2.50 ± 0.42	1.60 ± 0.18	1.96 ± 0.31	$2.4^{+1.0}_{-0.9} \times 10^{2}$

of the kinetic power spectrum with N, separately. The methodology applied is otherwise the same as discussed in §2.2 and §4.1. The fit parameters from fitting the decomposed power spectra are listed in Tab. B1.

Fig. B1 shows the longitudinal (transverse) kinetic power spectrum $P_{\mathrm{kin}_{\parallel}}$ ($P_{\mathrm{kin}_{\perp}}$) and its viscous dissipation wave number $k_{\nu_{\parallel}}$ ($k_{\nu_{\perp}}$) along with their fits for our series of simulations in the top (bottom) panels.

We start by noting some of the theoretical expectations for the longitudinal ($P_{\mathrm{kin}_{\parallel}}$) and transverse ($P_{\mathrm{kin}_{\perp}}$) components of P_{kin}. We emphasise that the transverse component is related to vorticity ($\nabla\times\mathbf{u}$), which is dominant on small scales, while the longitudinal component relates to compression in shocks, which are correlated on relatively larger scales.

We now discuss the resulting k_{ν} vs. N plots for the decomposed spectra (right panels of Fig. B1). Interestingly, for the longitudinal component ($k_{\nu_{\parallel}}$), we find that $p_{\mathrm{Re}} \sim 3/2$, as theoretically expected for Burgers turbulence (c.f., Eq. 22 and §4.1.2). For the transverse component, we find practically the same results as in the main text, where we do not do the Helmholtz decomposition, i.e., where we only consider the total kinetic power. This easy to understand, because most of the kinetic power is in the transverse component even for supersonic turbulence (see e.g., fig. 14, bottom left panel, in Federrath et al. 2010).

A possible explanation for the unexpected value of p_{Re} obtained from $k_{\nu_{\perp}}$ is that, in the supersonic regime, the rotating fluid components (that exist on small spatial scales) are encompassed within the shocks caused due to compression (occurring at larger spatial scales). Therefore, the geometry and isotropic nature of the vorticity elements get distorted due to the stretching and compression. Therefore, the behaviour of p_{Re} may differ even within a spatial scale.

We note that even though the transverse component of the kinetic spectra is primarily guided by the vorticity of fluid elements, it is not entirely incompressible, as there still exists a continuous exchange of energy between the transverse and longitudinal components, which influences the nature of $P_{\mathrm{kin}_{\perp}}$. Therefore, it is to be wondered what the ratio of contribution of 'purely' transverse and longitudinal components are to the nature of both P_{kin} and P_{mag}.

Therefore, we conclude by saying that our study, while mainly focusing on the dissipation range of the spectra, has introduced questions about the behaviour of the longitudinal and transverse components of energies and the resulting parameters, which requires further research.

APPENDIX C: RELATION BETWEEN p_{Re} AND p_{Rm}

Here we derive the relation between p_{Re} and p_{Rm}. Plugging Eq. (15) with $p_{\mathrm{Re}} = p_{\mathrm{Re_{theo}}}$, and Eq. (3) into Eq. (19), and using Eqs. (16) and (20), we find

$$k_{\eta} \propto k_{\nu}\mathrm{Pm}^{1/2}, \tag{C1}$$

$$\propto \mathrm{Re}^{1/p_{\mathrm{Re_{theo}}}} \left(\frac{\mathrm{Rm}}{\mathrm{Re}}\right)^{1/2}, \tag{C2}$$

$$\propto \mathrm{Re}^{\frac{2-p_{\mathrm{Re_{theo}}}}{2p_{\mathrm{Re_{theo}}}}}\,\mathrm{Rm}^{1/2}, \tag{C3}$$

$$\propto \left(\frac{N}{N_{\mathrm{Re}}}\right)^{p_{\mathrm{Re}}\frac{2-p_{\mathrm{Re_{theo}}}}{2p_{\mathrm{Re_{theo}}}}} \left(\frac{N}{N_{\mathrm{Rm}}}\right)^{\frac{p_{\mathrm{Rm}}}{2}}, \tag{C4}$$

$$\propto \frac{N^{\left(\frac{2-p_{\mathrm{Re_{theo}}}}{2p_{\mathrm{Re_{theo}}}}\right)p_{\mathrm{Re}}+\frac{p_{\mathrm{Rm}}}{2}}}{N_{\mathrm{Re}}^{\left(\frac{2-p_{\mathrm{Re_{theo}}}}{2p_{\mathrm{Re_{theo}}}}\right)p_{\mathrm{Re}}} + N_{\mathrm{Rm}}^{\frac{p_{\mathrm{Rm}}}{2}}}. \tag{C5}$$

As k_η varies linearly with N (see §4.1.2), the exponent of N in Eq. (C5) is unity. Therefore,

$$\left(\frac{2 - p_{\mathrm{Re_{theo}}}}{2p_{\mathrm{Re_{theo}}}}\right) p_{\mathrm{Re}} + \frac{p_{\mathrm{Rm}}}{2} = 1. \tag{C6}$$

For $\mathcal{M} = 0.1$, given $p_{\mathrm{Re_{theo}}} = \frac{4}{3}$, we find

$$\left(\frac{2 - \frac{4}{3}}{2 * \frac{4}{3}}\right) p_{\mathrm{Re}} + \frac{p_{\mathrm{Rm}}}{2} = 1, \tag{C7}$$

$$\frac{p_{\mathrm{Re}}}{4} + \frac{p_{\mathrm{Rm}}}{2} = 1, \tag{C8}$$

$$\implies p_{\mathrm{Rm}} = \frac{4 - p_{\mathrm{Re}}}{2}. \tag{C9}$$

Similarly, for $\mathcal{M} = 10$, with $p_{\mathrm{Re_{theo}}} = \frac{3}{2}$, we have

$$\left(\frac{2 - \frac{3}{2}}{2 * \frac{3}{2}}\right) p_{\mathrm{Re}} + \frac{p_{\mathrm{Rm}}}{2} = 1, \tag{C10}$$

$$\frac{p_{\mathrm{Re}}}{6} + \frac{p_{\mathrm{Rm}}}{2} = 1, \tag{C11}$$

$$\implies p_{\mathrm{Rm}} = \frac{6 - p_{\mathrm{Re}}}{3}. \tag{C12}$$

Therefore, we establish Eqs. (C9) and (C12) as the relation between p_{Re} and p_{Rm} in the subsonic and supersonic regimes, respectively.

APPENDIX D: RELATION BETWEEN p_{Re} AND p_{kin}

Here we derive the relation between p_{Re} and p_{kin}. We note that

$$P_{\mathrm{kin}}(k) \propto \frac{u_k^2}{k}, \tag{D1}$$

where u_k is the velocity of the fluid element at wave number k. As $P_{\mathrm{kin}}(k) \propto k^{p_{\mathrm{kin}}}$ (see Eq. 10), we can write

$$u_k^2 \propto k^{p_{\mathrm{kin}}+1}. \tag{D2}$$

In terms of the length scale (ℓ), this is equivalent to

$$u_\ell \propto \ell^{-(p_{\mathrm{kin}}+1)/2}. \tag{D3}$$

Now,

$$\mathrm{Re} = \frac{\ell u_\ell}{\nu} \propto \ell^{(1-p_{\mathrm{kin}})/2}, \tag{D4}$$

because $\nu = \mathrm{const.}$

We further have $N = \frac{\ell}{\ell_\nu}$, where $\ell_\nu = \frac{2\pi}{k_\nu}$, is the length scale at which viscous dissipation takes over in the kinetic spectrum P_{kin}.

Therefore, from Eq. (16), we find

$$\mathrm{Re} \propto \left(\frac{\ell}{\ell_\nu}\right)^{p_{\mathrm{Re}}} \propto \ell^{p_{\mathrm{Re}}}. \tag{D5}$$

Thus, from Eqs. (D4) and (D5), we find

$$p_{\mathrm{Re}} = \frac{1 - p_{\mathrm{kin}}}{2}. \tag{D6}$$

This paper has been typeset from a TEX/LATEX file prepared by the author.